

---

## Estimation of Horizontal Turbulent Diffusivity from Deep Argo Float Displacements

Sévellec Florian <sup>1,\*</sup>, Colin De Verdière Alain <sup>2</sup>, Kolodziejczyk Nicolas <sup>2</sup>

<sup>1</sup> Laboratoire d'Océanographie Physique et Spatiale, Univ-Brest CNRS IRD Ifremer, Brest, France  
Ocean and Earth Sciences, University of Southampton, Southampton, UK

<sup>2</sup> Laboratoire d'Océanographie Physique et Spatiale, Univ-Brest CNRS IRD Ifremer, Brest, France

\* Corresponding author : Florian Sévellec, email address : [florian.sevellec@univ-brest.fr](mailto:florian.sevellec@univ-brest.fr)

---

### Abstract :

We use an analog method, based on displacements of Argo floats at their parking depth (nominally located around 1,000 dbar) from ANDRO dataset, to compute continuous, likely trajectories and estimate the Lagrangian dispersion. From this, we find that the horizontal diffusivity coefficient has a median value around 500 m<sup>2</sup> s<sup>-1</sup> but is highly variable in space: reaching values from 100 m<sup>2</sup> s<sup>-1</sup> in gyre interior to 40,000 m<sup>2</sup> s<sup>-1</sup> in a few specific locations (in the Zapiola gyre and in the Agulhas Current retroflexion). Our analysis suggests that the closure for diffusivity is proportional to Eddy Kinetic Energy (or square of turbulent velocity) rather than (absolute) turbulent velocity. It is associated to a typical turbulent time scale of 4 to 5.5 days, which is noticeably quite constant over the entire globe, especially away from coherent intense currents. The diffusion is anisotropic in coherent intense currents and around the equator, with a primary direction of diffusion consistent with the primary direction of horizontal velocity variance. These observationally based horizontal diffusivity estimations, and the suggested Eddy Kinetic Energy closure, can be used for constraining, testing, and validating eddy turbulence parameterization.

## 1 Introduction

Horizontal ocean mixing by mesoscale eddies and submesoscale processes has a wide variety of impacts from the dispersion of pollutants, to nutrients and ecosystem resources, to sequestration of heat and (anthropogenic) carbon, to variation in ocean heat content, to distributions of water mass properties, to the maintenance of the large scale ocean circulation (Wunsch, 1999). Consequently, mixing process imprint occurs from the large scale ocean current (e.g., abyssal circulation, de Lavergne et al., 2016) to water mass transformation and ventilation (e.g., Upper Circumpolar Deep Water and global ocean, Zika et al., 2020; Portela et al., 2020a,b), to regional and local dynamics (e.g., coastal upwelling systems, Capet et al., 2013). Hence evaluating the horizontal mixing in the ocean is one of the overarching question of current ocean physics, with consequences for climate dynamics and for biogeochemical tracer dynamics.

The whole subject of dispersion of fluid particles from fixed origin, the so called absolute dispersion, originates from Taylor (1921) who showed the link between the dispersion and the Lagrangian velocity correlation function. Batchelor (1949) formalized the result in several dimensions and showed how to relate the particle statistics and the diffusion equation for a passive tracer when the probability distribution of the displacements of a fluid particle is Gaussian. A modern discussion of these issues is provided by Davis (1987, 1991) within the context of oceanic float observations. This framework was further used to describe ocean eddy flux closure with the use of Lagrangian float velocities (Garrett, 2006). More recently, Klocker et al. (2012) discussed the link between float-based and tracer-based estimates of lateral diffusivity. An example of this diffusivity computation based on surface oceanic observations can be found in Klocker and Abernathey (2014) and Zhurbas et al. (2014). In parallel to these studies, Ying et al. (2019) suggested the use of Bayesian approach to infer diffusivity from Lagrangian trajectories in an idealized ocean circulation setting. There has also been a large range of numerical studies, using Lagrangian particles within high resolu-

tion ocean modelling, whose goal is to assess the ocean (sub-surface) diffusivity coefficients (e.g., Balwada et al., 2021) and to test different closure schemes (e.g., Chen et al., 2015). We refer the reader to van Sebille et al. (2018) for an exhaustive review on Lagrangian ocean analyses and to LaCasce (2008) for a thorough review on diffusivity computation, the different methodologies, and their shortcomings.

Following the use of Lagrangian floats for the MODE Experiment in 1973 (located in the southwest of the North Atlantic subtropical gyre), local estimates of horizontal eddy diffusivities started to be obtained from the rate of dispersion of floats at depth ranging from 700 m to 1,500 m (Freeland et al., 1975; Riser and Rossby, 1983; Rossby et al., 1983; Böning, 1988, for a summary). Overall, these studies reported values from slightly below  $1,000 \text{ m}^2 \text{ s}^{-1}$  to almost  $5,000 \text{ m}^2 \text{ s}^{-1}$ , with a large degree of uncertainties. Ollitrault and Colin de Verdière (2002) reported values of the same magnitude, but suggested a high spatial variability (i.e.,  $5,000 \text{ m}^2 \text{ s}^{-1}$  and  $2,200 \text{ m}^2 \text{ s}^{-1}$  west and east of the Mid-Atlantic Ridge, respectively). Other regions have also been explored. In the Southern Ocean, west of the Drake passage (i.e., upstream of the Antarctic Circumpolar Current), LaCasce et al. (2014) and Tulloch et al. (2014) reported  $800 \pm 200 \text{ m}^2 \text{ s}^{-1}$  (at 950 m depth) and  $710 \pm 260 \text{ m}^2 \text{ s}^{-1}$  (at 1,500 m depth), respectively. It is interesting to note that these Southern Ocean values are relatively low compared to the values reported for the North Atlantic Western basin, whereas the, *a priori*, eddy activity is similar, if not more intense, in the former region than the latter region.

There also exists indirect estimates of horizontal diffusivity coefficients. For instance, Cole et al. (2015) used a mixing length argument (obtained through salinity anomalies and mean gradient) to infer diffusivities at the base of the mixed layer. They reported highly spatially-varying values from a few  $100 \text{ m}^2 \text{ s}^{-1}$  to several  $10,000 \text{ m}^2 \text{ s}^{-1}$ . This particular study has the advantage of a global coverage, but the diffusivity coefficients are inherently dependent on the validity of the mixing length argument.

Thus, a full description of the diffusivity coefficients at depth, must rely on direct *in situ* observations either passive tracers or particle trajectories. However, this presents difficulties, which comes in twofold. On the one hand, tracking the evolution of the release of a passive tracer concentration requires repeated observations over a large oceanic region (e.g., Tulloch et al., 2014) and accurately sampling the concentration is challenging, requiring a vast amount of resources (in terms of scientific cruises). On the other hand, the diffusivity can be obtained using the spread of an ensemble of Lagrangian float trajectories with a high degree sampling obtained from acoustic navigation (see review by LaCasce et al., 2014), but this method requires the use of a large number of acoustic floats (e.g., SOFAR or RAFOS) dedicated to the study. An other limitation of these methods is that their results are local and impossible to generalize at basin scales. Here we circumvent these issues by using the Argo deep displacements, which is a huge database with a global coverage. This approach has already been suggested by Roach et al. (2018) for computing decorrelated pair-dispersion. However to assess the diffusivity from the Argo observations a major difficulty must be overcome, namely the fact that Argo floats subsample the path of water parcels at 10-day intervals only. Despite being fully acknowledged, this important difficulty was not treated in Roach et al. (2018). Here we suggest a new methodology to overcome it.

In this study we apply an analog method (Ayet and Tandeo, 2018) to reconstruct pseudo-trajectories that are continuous (in space and time) and possess the local statistical properties of Argo float displacements. The dispersion of these “likely”, continuous trajectories is used to infer the horizontal diffusivity coefficients at 1,000-m depth. We find that diffusivities vary significantly between hot spot regions, with values ranging from  $1,000 \text{ m}^2 \text{ s}^{-1}$  to several  $10,000 \text{ m}^2 \text{ s}^{-1}$ , and gyre interiors, with values ranging from a few  $100 \text{ m}^2 \text{ s}^{-1}$  to  $1,000 \text{ m}^2 \text{ s}^{-1}$ . Testing turbulent closures, we find that the diffusivity scales well with the Eddy Kinetic Energy (squared velocities), giving a turbulent time scale of 4 to 5.5 days nearly constant globally. We also show that the regions of high Eddy Kinetic Energy are associated with

anisotropic diffusion, the primary direction for diffusion being aligned with the primary direction of horizontal velocity variance (i.e., the main eigenvector of the horizontal velocity covariance matrix).

The manuscript is organized as follows. The observational data, the analog method used to reconstruct continuous Lagrangian pseudo-trajectories, and the method for deriving the diffusivity coefficients are described in section 2. Section 3 presents the geography of diffusivity coefficients and the possible scaling with two classical turbulent closures. Discussions and conclusions are included in section 4.

## 2 Data and Method

### *a. The ANDRO Dataset*

The horizontal turbulent diffusivities is computed through the dispersion of Lagrangian particles following horizontal deep displacements of Argo floats. These displacements are obtained from the ANDRO dataset (Ollitrault et al., 2019). For details on the ANDRO dataset we refer the reader to Ollitrault and Rannou (2013), Ollitrault and Colin de Verdière (2014), Colin de Verdière and Ollitrault (2016), Sévellec et al. (2017), and Colin de Verdière et al. (2019). The ANDRO dataset gives access to 1,041,054 displacements prior to 31<sup>st</sup> October 2017. Numerous checks are used to validate and correct Argo parking pressure in order to determine the reference parking pressure and to remove incorrect nominal parking depth recorded in the metadata. Additional control is performed to report float grounding that prevent accurate estimation of parking depth and drift velocity. The dataset is particularly well suited for estimating displacement at depth by providing the last surface transmitted position and time before diving, the first transmitted position and time after surfacing.

From this dataset, the first step of our study was to eliminate data flagged as erroneous and to restrict displacements lasting  $\sim 10$  days and located at  $\sim 1,000$  dbar. This leads to a total number of displacements of 675,575 (Fig. 1).

Despite having a consistent set of displacements, there are still a few sources of error:

- Parking pressures are selected within the range between 950 and 1,150 dbar. However most of the displacements occur close to 1,000 dbar with a standard deviation of only 22 dbar. Thus we assume this error to be negligible.
- Drifting time periods at depth ( $\Delta t_{\text{deep}}$ ) are estimated as the differences between  $t_i$  and  $t_f$  (the last position time before diving and the first position time after surfacing, respectively). They are selected in a finite range between 8.5 and 10.5 days leading to standard deviation of only 0.36 days. In the following we will consider that periods as the mean of that distribution, that is 9.74 days exactly.
- However, since both  $t_i$  and  $t_f$  are determined at the surface, the actual drift at depth will be biased due to the current shear between the surface and the parking depth. This leads to an error of a few km (less than 5 km for 90% of the displacements), using both the surface and deep approximate velocities (Ollitrault and Rannou, 2013). There is also on average an error of 1 to 2 km due to typical one hour delay between the last surface position time and the diving time or between the surfacing time and the first surface position time (most floats are positioned by the Argos satellite system). In conclusion, we can assume on average a possible error on an individual displacement of 5 km, which remains small compared to the 10-day typical displacements.
- Beyond that, the 10-day displacements lead to the undersampling of motions above the Nyquist frequency of  $1/(2\Delta t_{\text{deep}}) \simeq 1/20$  cycles per day.

Before using the data set it is important to look at the coverage density of Argo float displacements (Fig. 1c). Displacements are recorded everywhere in the ocean, but the coverage remains inhomogeneous: there is relative undersampling in the Southern Ocean and equatorial Pacific and a relative oversampling in the subtropical gyres of the Pacific, Atlantic

and Indian oceans. The density of selected Argo float displacements for our  $3^\circ \times 3^\circ$  grid has an average value of 171 per  $3^\circ \times 3^\circ$  with a standard deviation of 36 per  $3^\circ \times 3^\circ$ , but can locally go up to 732 per  $3^\circ \times 3^\circ$ .

Difference between two float displacements starting from two close locations could be due to (permanent) spatial difference between the flow of the two starting locations, to time variations of the flow between the first displacement and the second displacement, or to both. In this study, these types of displacement differences are aggregated in the same statistics.

A complete error estimation of a subset of the ANDRO dataset used here (i.e., a prior version) was provided in Sévellec et al. (2017). They demonstrated the good accuracy for experiments on timescales of a few months, relevant for our current study.

The ANDRO dataset, also provides corrected zonal and meridional deep velocities computed from the individual displacements and their time periods at depths (Ollitrault and Rannou, 2013; Ollitrault et al., 2019). This corresponds to a set of localized 10-day integrated velocities. From these, the mean velocity can be computed each  $1^\circ \times 1^\circ$  using a running average of all velocities over a  $3^\circ \times 3^\circ$  grid as:

$$\bar{u}(x_0, y_0) = \frac{1}{n} \sum_{j=1}^n u_j(x, y)|_{\mathcal{O}(x_0, y_0)}, \quad (1a)$$

$$\bar{v}(x_0, y_0) = \frac{1}{n} \sum_{j=1}^n v_j(x, y)|_{\mathcal{O}(x_0, y_0)}, \quad (1b)$$

where  $\bar{u}$  and  $\bar{v}$  are the zonal and meridional mean velocities, respectively;  $u_j$  and  $v_j$  are the zonal and meridional velocities from the ANDRO dataset, respectively;  $x$  and  $y$  are the longitude and latitude, respectively;  $\mathcal{O}(x_0, y_0)$  defines a box centered at longitude  $x_0$  and latitude  $y_0$  such as:  $x \in [x_0 - \frac{1}{2}\Delta x, x_0 + \frac{1}{2}\Delta x]$  and  $y \in [y_0 - \frac{1}{2}\Delta y, y_0 + \frac{1}{2}\Delta y]$  with  $x_0$  and  $y_0$  are evenly space every  $1^\circ$ , and  $\Delta x$  and  $\Delta y$  are the zonal and meridional extend of the spatial mean corresponding to  $3^\circ \times 3^\circ$  box, respectively;  $n$  is the number of zonal and meridional velocity sample available in this  $\mathcal{O}$  box; and  $j$  is the index of these individual velocities. It is important to acknowledge that this Lagrangian velocity mean slightly differs from the more

classical Eulerian velocity mean (Wang et al., 2020).

The mean velocities show the expected circulation at this depth (Fig 2a and b). The circulation is dominated by an intense eastward flow in the Southern Ocean, characteristic of the Antarctic Circumpolar Current. The flow also shows signature of intense boundary currents such as the Gulf Stream, Kuroshio, and Falkland Current, for instance.

The turbulent velocities and covariance velocity can also be estimated at each  $1^\circ \times 1^\circ$  as the standard deviation of all the velocities recorded in the ANDRO dataset within a  $3^\circ \times 3^\circ$  grid. This reads:

$$\tilde{u}(x_0, y_0) = \sqrt{\frac{1}{n} \sum_{j=1}^n \left[ u_j(x, y)|_{\mathcal{O}(x_0, y_0)} - \bar{u} \right]^2}, \quad (2a)$$

$$\tilde{v}(x_0, y_0) = \sqrt{\frac{1}{n} \sum_{j=1}^n \left[ v_j(x, y)|_{\mathcal{O}(x_0, y_0)} - \bar{v} \right]^2}, \quad (2b)$$

$$\tilde{c}^2(x_0, y_0) = \frac{1}{n} \sum_{j=1}^n \left[ u_j(x, y)|_{\mathcal{O}(x_0, y_0)} - \bar{u} \right] \left[ v_j(x, y)|_{\mathcal{O}(x_0, y_0)} - \bar{v} \right], \quad (2c)$$

where  $\tilde{u}$  and  $\tilde{v}$  are the zonal and meridional turbulent velocities, respectively; and  $\tilde{c}^2$  is the covariance velocity. It is worth noting that  $\tilde{u}^2 + \tilde{v}^2$  is twice the Eddy Kinetic Energy. Note that with this definition the turbulent velocities are not strictly restricted to mesoscale eddy turbulence and submesoscale processes, there could be a component linked to slower variability.

For both turbulent velocities, the computation shows intensification in western boundary currents and along the Antarctic Circumpolar Current (Fig. 2c and d), as expected in regions of active turbulent mesoscale activity. The regions of the Zapiola Gyre and of the Agulhas Current retroflexion are also particularly noticeable. For the zonal turbulent velocities, the equatorial band also appears to be quite active. We interpret that as the signature of the meridional shear of zonal velocities induced by the succession of, possibly steady, equatorial currents and countercurrents in the vicinity of the equator and of waves propagating along the equator at depth (Delpech et al., 2020). For the meridional turbulent velocities an interesting

region is the Somali Current (Schott et al., 2009). The intermittent behavior of the current is reflected in the meridional turbulent velocities (which does not distinguish between spatial and temporal variability).

Note that zonal and meridional mean and turbulent velocities, as well as the covariance velocity, appear independent of the tested grid resolution (i.e.,  $\Delta x$  and  $\Delta y$  varying from  $2^\circ$  to  $5^\circ$ ), beyond the typical smoothing expected with larger grid representation. It is also interesting to note that, as expected (Wunsch and Ferrari, 2018), the ratio of the mean to the standard deviation is almost always small, suggesting the small Péclet number (i.e., ratio of the mean advection to the turbulent advection) of the coarse  $3^\circ \times 3^\circ$  1,000-m depth flow.

#### *b. The Analog Method for Lagrangian Trajectories*

Given that Argo floats resurface every  $\sim 10$  days (which is of the order of the Lagrangian integral time scale, as suggested by local *in situ* observational analyses of the North Atlantic, Freeland et al., 1975; Rossby et al., 1983; Ollitrault and Colin de Verdière, 2002), the record of their journey at depth is discontinuous. This is problematic for estimating horizontal diffusivities, which require continuous trajectories. To overcome this central difficulty, continuous pseudo-trajectories are reconstructed in the following way. We use the analog methodology which has been applied successfully in various fields from solar irradiance forecast (Ayet and Tandeo, 2018) to interannual climate prediction (Sévellec and Drijfhout, 2018), for instance. The objective of the method is to produce continuous, likely trajectories, whose 10-day displacements are analog to those recorded in the ANDRO dataset. To this purpose the displacements of likely trajectory will come in two parts, one deterministic accounting for the mean flow and the other random acknowledging the turbulent part of the flow. To sample the randomness, 100 trajectories are computed from each starting position, evenly spaced on a  $1^\circ \times 1^\circ$  grid. (100 trajectories were shown to be enough to capture accurately the ensemble mean and variance of the trajectories.)

The mean zonal and meridional displacements are computed as the average zonal and meridional displacements, respectively, recorded within the ANDRO dataset over a  $3^\circ \times 3^\circ$  box centered at the location of the estimation. For the random components the possible outcomes follows the meridional and zonal variance. We assume that they are fully independent between time iterations and member realizations, but we acknowledge the observed covariance between the zonal and meridional displacement components. This choice assumes that the distribution of the zonal and meridional displacements follow a normal distribution (as suggested by Ollitrault and Colin de Verdière, 2002; LaCasce, 2008, and fully tested later in the section 2c.), which is well captured by only knowing the mean and the standard deviation. The standard deviation is also estimated over the same  $3^\circ \times 3^\circ$  box centered at the location of the estimation. Hence both mean and random components of a displacement are estimated using the neighboring flow properties changing along the trajectory path of the analog particle.

Other strategies exist to set the range of analog displacements. It is sometime set to a constant number, regardless of the distance. Alternatively, one could set a spatial range linked to dynamical parameter, such as the Rossby deformation radius. Here, and as mentioned above, we simply set a spatially constant range of  $3^\circ \times 3^\circ$ . (Note that we have also tested  $5^\circ \times 5^\circ$ , as discussed later.)

Following our suggested uniform-grid framework, the position of likely trajectories can be expressed mathematically as:

$$\begin{pmatrix} \widehat{dx}_i \\ \widehat{dy}_i \end{pmatrix} = \begin{pmatrix} \overline{dx} \\ \overline{dy} \end{pmatrix} + \mathbf{L} \begin{pmatrix} r_{xx} \\ r_{xy} \end{pmatrix}, \quad (3a)$$

$$\begin{pmatrix} x_i^{\text{new}} \\ y_i^{\text{new}} \end{pmatrix} = \begin{pmatrix} x_i^{\text{old}} \\ y_i^{\text{old}} \end{pmatrix} + \begin{pmatrix} \widehat{dx}_i \\ \widehat{dy}_i \end{pmatrix} - \begin{pmatrix} \frac{1}{N} \sum_i^N \widehat{dx}_i \\ \frac{1}{N} \sum_i^N \widehat{dy}_i \end{pmatrix}, \quad (3b)$$

where  $\widehat{dx}_i$  and  $\widehat{dy}_i$  are the reconstructed longitude and latitude 10-day displacements of the  $i^{\text{th}}$  reconstructed trajectory, respectively,,  $x_i^{\text{old}}$ ,  $y_i^{\text{old}}$ ,  $x_i^{\text{new}}$ , and  $y_i^{\text{new}}$  are the old and new

longitude and latitude prior and after the 10-day displacement of the  $i^{\text{th}}$  reconstructed trajectory, respectively,  $N$  ( $=100$ ) is the number of ensemble member,  $i$  the index of the ensemble member,  $\overline{dx} = \frac{1}{n} \sum_{j=1}^n dx_j|_{\mathcal{O}(x_i^{\text{old}}, y_i^{\text{old}})}$  and  $\overline{dy} = \frac{1}{n} \sum_{j=1}^n dy_j|_{\mathcal{O}(x_i^{\text{old}}, y_i^{\text{old}})}$  are the local mean of zonal and meridional displacements with a starting location within a  $3^\circ \times 3^\circ$  box centered at  $(x_i^{\text{old}}, y_i^{\text{old}})$ , respectively (where  $dx_j$  and  $dy_j$  are individual zonal and meridional displacements as recorded by ANDRO dataset, respectively),  $r_{xx}$  and  $r_{xy}$  are two independent random outcomes of two centered unit-variance normal distributions that impact only the zonal and both zonal and meridional displacements, respectively, and  $\mathbf{L}$  is a lower triangular matrix outcome of the Cholesky factorization of the symmetric positive definite covariance displacement matrix ( $\mathbf{D}$ ), such that  $\mathbf{D} = \mathbf{L}\mathbf{L}^\dagger$  (where  $\dagger$  denotes the transpose operator). The covariance displacement matrix reads:

$$\mathbf{D} = \begin{pmatrix} D_{xx} & D_{xy} \\ D_{xy} & D_{yy} \end{pmatrix},$$

$$= \begin{pmatrix} \frac{1}{n} \sum_{j=1}^n (dx_j - \overline{dx})^2 \Big|_{\mathcal{O}(x_i^{\text{old}}, y_i^{\text{old}})} & \frac{1}{n} \sum_{j=1}^n (dx_j - \overline{dx})(dy_j - \overline{dy}) \Big|_{\mathcal{O}(x_i^{\text{old}}, y_i^{\text{old}})} \\ \frac{1}{n} \sum_{j=1}^n (dx_j - \overline{dx})(dy_j - \overline{dy}) \Big|_{\mathcal{O}(x_i^{\text{old}}, y_i^{\text{old}})} & \frac{1}{n} \sum_{j=1}^n (dy_j - \overline{dy})^2 \Big|_{\mathcal{O}(x_i^{\text{old}}, y_i^{\text{old}})} \end{pmatrix}.$$

We can therefore write the Cholesky factorization as:

$$\mathbf{L} = \begin{pmatrix} \sqrt{D_{xx}} & 0 \\ \frac{D_{xy}}{\sqrt{D_{xx}}} & \sqrt{D_{yy} - \frac{D_{xy}^2}{D_{xx}}} \end{pmatrix}.$$

This ensures that the variances of the zonal and meridional displacements, as well as their covariance, are consistent with values observed in the ANDRO database.

The mathematical procedure described in (3) implies that the new position will be given by the sum of the old position, the mean displacement measured in the  $3^\circ \times 3^\circ$  box neighborhood, a random component varying for each trajectory and based on the covariance displacement measured in the  $3^\circ \times 3^\circ$  box neighborhood, and subtracting the mean displacement of the trajectory ensemble (see discussion below).

Hence, replacing  $(x_i^{\text{old}}, y_i^{\text{old}})$  by  $(x_i^{\text{new}}, y_i^{\text{new}})$  sequentially and reevaluating  $(\overline{dx}, \overline{dy}, r_{xx},$  and  $r_{xy})$  in (3) provide a continuous trajectory. Through this analog method we can reproduce continuous, likely trajectories (Fig. 3) with statistical properties, in term of zonal and meridional displacements, virtually identical from those of Argo floats during their journey at depth. Since the  $3^\circ \times 3^\circ$  box neighborhood, used to compute the statistical properties of the displacements, evolves with the trajectory increment, this analog method is adaptative in time. This differs from the transfer operator method, used in a previous study by the authors (Sévellec et al., 2017), which had a fix grid and potentially lead to spurious diffusion, making it less reliable to measure accurately the observed diffusion.

As mentioned above, the ensemble mean displacement is removed from each individual displacements. This allows the mean ensemble to remain at the same location and restrict the evolution of the ensemble to its spread alone. This facilitates a more robust use of the diffusion equation  $(\partial_t C = \nabla \cdot \mathbf{K} \cdot \nabla C$ , where  $C$  is a concentration and  $\mathbf{K}$  is a horizontal diffusivity tensor) central to our diffusivity estimations, which should be modified in presence of a mean flow into an advection-diffusion equation  $(D_t C = \nabla \cdot \mathbf{K} \cdot \nabla C$ , where  $D_t$  is the material “mean” derivative). (Note that we also accurately assume the absence of source terms in both formulations.) Hence, by removing the mean displacement, we compute a diffusivity specific to a local area. Also it allows us to compute the diffusivity coefficients in both horizontal directions without being restricted to the cross-mean flow direction. The along-mean flow direction is often more difficult to extract because of the impact of the shear of the mean flow (LaCasce et al., 2014). However, as discussed in the previous subsection the flow is mostly dominated by its turbulent component rather than its mean component, on the coarse  $3^\circ \times 3^\circ$  gridded dynamics. Hence, our tests suggest that, despite allowing the more accurate computation of local diffusivities (vs diffusivities computed along the track of the mean flow), the removal of the mean ensemble displacement is not fundamental, in most places, and does not modify significantly the quantitative results discussed in the rest of the

study. (We refer the readers to section 4 for a discussion on the Southern Ocean, an example of regions where this choice matters.)

*c. Test of the Normal Assumption and of the Spatial Discretization Resolution*

As mentioned above, this analog computation procedure implies a fundamental assumption: the displacements can be represented by a normal distribution. To test it, we define the Shannon Entropy ( $H$ ) and Kullback-Leibler divergence ( $D_{\text{KL}}$ ). The former measures the information of the observed probability density distribution of the zonal or meridional displacements ( $P_{dX}$  or  $P_{dY}$ , respectively) as

$$H(dX) = - \sum_j P_{dX}(dx_j) \ln [P_{dX}(dx_j)], \quad (4a)$$

$$H(dY) = - \sum_j P_{dY}(dy_j) \ln [P_{dY}(dy_j)], \quad (4b)$$

where  $\ln$  is the natural logarithm, and  $dX$  and  $dY$  are the discrete random variables of possible outcomes  $dx_j$  and  $dy_j$  for the zonal and meridional displacements, respectively. The distributions are evaluated through 20 bins evenly space within plus/minus the maximum absolute displacements. Whereas the latter measures the missing information from theoretical Gaussian fits ( $Q_{dX}$  or  $Q_{dY}$ , respectively, representing a normal distribution of equivalent mean and standard deviation than  $P_{dX}$  or  $P_{dY}$ ) to the observed probability density distributions. It reads:

$$D_{\text{KL}}(P_{dX}||Q_{dX}) = \sum_i P_{dX}(dx_i) \ln \left[ \frac{P_{dX}(dx_i)}{Q_{dX}(dx_i)} \right], \quad (5a)$$

$$D_{\text{KL}}(P_{dY}||Q_{dY}) = \sum_j P_{dY}(dy_j) \ln \left[ \frac{P_{dY}(dy_j)}{Q_{dY}(dy_j)} \right]. \quad (5b)$$

Hence we can define the relative Missing Information index (MI) as  $\text{MI} = D_{\text{KL}}/H$ . This error estimation demonstrates that the assumption of a normal distribution appears to be highly adequate both for the zonal and meridional directions. The relative error is weaker than 5% over almost the entire globe, except a few specific locations and along coastlines (Fig. 4).

This coastal issue is likely to come from the lack of observations over the  $3^\circ \times 3^\circ$  box centered at these coastal locations (i.e., lack of recorded displacements over land and in regions of bathymetry higher than 1,000 dbar).

Previous studies have suggested the deviation of the velocity distribution from the normal distribution, particularly related to rare but energetic events (e.g., Bracco et al., 2000; Pasquero et al., 2001). In our dataset such deviation appear to be weak (Fig. 4), however if such deviation exist it would have implication in the formulation of (3), which would need to be revised to acknowledge higher order statistical moments

To test the robustness of the discretization (or spatial range over which analogs are computed) at the heart of the analog method, a  $5^\circ \times 5^\circ$  grid has also been tested. It did not show significantly different results from the  $3^\circ \times 3^\circ$  grid. (The difference in computed diffusivities is discussed in section 3b.). This does not show major impact of the discretization, beyond the expected smoothing linked to the use of coarser/larger grid. It is worth noting that, with our analog method, the discretization is not a spatial-averaging but a spatial-range over which the statistical properties of the observed trajectories are aggregated (especially to compute the second central moment). Hence the discretization for Argo displacements does not act as a spatial-filter of physical processes, as typically done in numerical modelling with eddy-less/laminar model (e.g.,  $2^\circ \times 2^\circ$ ), eddy-permitting model (e.g.,  $1/4^\circ \times 1/4^\circ$ ), or eddy-resolving model (e.g.,  $1/12^\circ \times 1/12^\circ$ ).

#### *d. Computing the Horizontal Diffusivity Coefficients*

Now that we have continuous, likely trajectories from analog displacements. We will compute the dispersion of trajectories initialized at the exact same location to infer the diffusivities at that depth. To this purpose, we first need to identify a relation between the trajectories, or their evolution, and diffusivities. This particular derivation strongly follows Batchelor (1949) and is described here for completeness to give the readers the full details of the calculations.

Hence, to determine the diffusivities, we restart from the diffusion equation described earlier which governs the tracer concentration simulated by our trajectories:  $\partial_t C = \nabla \cdot \mathbf{K} \cdot \nabla C$ . The horizontal diffusivity tensor can be represented by a symmetric matrix as:

$$\mathbf{K} = \begin{pmatrix} \kappa_{xx} & \kappa_{xy} \\ \kappa_{xy} & \kappa_{yy} \end{pmatrix},$$

where  $\kappa_{xx}$ ,  $\kappa_{yy}$ , and  $\kappa_{xy}$  are the zonal, meridional, and cross diffusivities. Assuming that the diffusivity coefficients do not spatially-vary over the region of evaluation (i.e., the region over which our simulated concentration spread) we have:

$$\partial_t C = \kappa_{xx} \partial_{xx}^2 C + 2\kappa_{xy} \partial_{xy}^2 C + \kappa_{yy} \partial_{yy}^2 C. \quad (6)$$

This local homogeneity assumption is essential to our study.

To compute the spread we will use a spatial integral defined over the spreading of the concentration and denoted by  $\langle \cdot \rangle$ . Since there is no concentration or flux away from the concentration/spreading-area we have  $\langle \partial_x(\dots) \rangle = \langle \partial_y(\dots) \rangle = 0$  and  $\langle \partial_{xx}^2(\dots) \rangle = \langle \partial_{yy}^2(\dots) \rangle = 0$ , respectively. Although less straightforward, we also have the useful properties:

$$\begin{aligned} \langle x^2 \partial_{xx} C \rangle &= \langle \partial_{xx} (x^2 C) \rangle - 2 \langle x \partial_x C \rangle, \\ &= \langle \partial_{xx} (x^2 C) \rangle - \langle \partial_x (xC) \rangle + 2 \langle C \rangle, \\ &= 0 - 0 + 2 \langle C \rangle; \end{aligned} \quad (7a)$$

$$\begin{aligned} \langle y^2 \partial_{yy} C \rangle &= \langle \partial_{yy} (y^2 C) \rangle - 2 \langle y \partial_y C \rangle, \\ &= \langle \partial_{yy} (y^2 C) \rangle - \langle \partial_y (yC) \rangle + 2 \langle C \rangle, \\ &= 0 - 0 + 2 \langle C \rangle; \end{aligned} \quad (7b)$$

$$\begin{aligned} \langle xy \partial_{xy} C \rangle = \langle x \partial_x (y \partial_y C) \rangle &= \langle \partial_x (xy \partial_y C) \rangle - \langle y \partial_y C \rangle, \\ &= \langle \partial_x (xy \partial_y C) \rangle - \langle \partial_y (yC) \rangle + \langle C \rangle, \\ &= 0 - 0 + \langle C \rangle. \end{aligned} \quad (7c)$$

Finally, defining the zonal and meridional distance to the steady (by construction) center of mass as  $\tilde{x}=(x - x_0)$  and  $\tilde{y}=(y - y_0)$ , respectively, we can define the zonal, meridional and co- variance as  $\text{var}_{xx}(C)=\langle\tilde{x}^2C\rangle/\langle C\rangle$ ,  $\text{var}_{yy}(C)=\langle\tilde{y}^2C\rangle/\langle C\rangle$ , and  $\text{var}_{xy}(C)=\langle\tilde{x}\tilde{y}C\rangle/\langle C\rangle$ , respectively. Using these definitions and (7), we can derive from (6) the evolution of the variances, which reads:

$$\begin{aligned}\partial_t\langle\tilde{x}^2C\rangle &= \kappa_{xx}\langle\tilde{x}^2\partial_{xx}^2C\rangle, \\ &= 2\kappa_{xx}\langle C\rangle, \\ \partial_t\text{var}_{xx}(C) &= \partial_t\frac{\langle\tilde{x}^2C\rangle}{\langle C\rangle} = 2\kappa_{xx};\end{aligned}\tag{8a}$$

$$\begin{aligned}\partial_t\langle\tilde{y}^2C\rangle &= \kappa_{yy}\langle\tilde{y}^2\partial_{yy}^2C\rangle, \\ &= 2\kappa_{yy}\langle C\rangle, \\ \partial_t\text{var}_{yy}(C) &= \partial_t\frac{\langle\tilde{y}^2C\rangle}{\langle C\rangle} = 2\kappa_{yy};\end{aligned}\tag{8b}$$

$$\begin{aligned}\partial_t\langle\tilde{x}\tilde{y}C\rangle &= 2\kappa_{xy}\langle\tilde{x}\tilde{y}\partial_{xy}^2C\rangle, \\ &= 2\kappa_{xy}\langle C\rangle, \\ \partial_t\text{var}_{xy}(C) &= \partial_t\frac{\langle\tilde{x}\tilde{y}C\rangle}{\langle C\rangle} = 2\kappa_{xy}.\end{aligned}\tag{8c}$$

To apply these formulas in the context of our Lagrangian pseudo-trajectories, we have initialized 100 trajectories each  $1^\circ\times 1^\circ$  all over the ocean and track them for 3 months. Then the estimation of the diffusivities has been done in two steps: (1) computation of the variances and (2) computation of the diffusivities.

1. From the trajectory dispersion, we compute the variances of ensemble trajectories along the zonal and meridional directions, and for the cross term. These variances read:

$$\sigma_{xx}^2(x_0, y_0, t) = \frac{1}{N} \sum_{i=1}^N [x_i^{x_0, y_0}(t) - x_0]^2, \tag{9a}$$

$$\sigma_{yy}^2(x_0, y_0, t) = \frac{1}{N} \sum_{i=1}^N [y_i^{y_0, y_0}(t) - y_0]^2, \tag{9b}$$

$$\sigma_{xy}^2(x_0, y_0, t) = \frac{1}{N} \sum_{i=1}^N [x_i^{y_0, y_0}(t) - x_0] [y_i^{y_0, y_0}(t) - y_0], \quad (9c)$$

where  $\sigma_{xx,yy,xy}^2$  are the zonal, meridional, and co- variance,  $t$  is time ( $=k\Delta t_{\text{deep}}$ , where  $k \in \mathbb{N}_0$ ),  $x_0$  and  $y_0$  are the longitude and latitude of the initialization location, and  $x_i^{x_0, y_0}$  and  $y_i^{x_0, y_0}$  are the longitude and latitude of the  $i^{\text{th}}$  trajectory member, initialized at  $[x_0, y_0]$ . Note that, in this formulation, we use the property that the mean ensemble position is constant and sets by construction of the continuous, likely trajectories at the location of the initialization ( $x_0$  and  $y_0$ ).

2. Then, using (8) and (9) together, the computation of the zonal, meridional, and cross diffusivities reads:

$$\kappa_{xx}(x_0, y_0) = \frac{1}{2} \frac{d}{dt} \sigma_{xx}^2(x_0, y_0, t); \quad (10a)$$

$$\kappa_{yy}(x_0, y_0) = \frac{1}{2} \frac{d}{dt} \sigma_{yy}^2(x_0, y_0, t); \quad (10b)$$

$$\kappa_{xy}(x_0, y_0) = \frac{1}{2} \frac{d}{dt} \sigma_{xy}^2(x_0, y_0, t). \quad (10c)$$

This last step is done through a best linear fit using 11 values uniformly distributed over a  $\sim 3$ -month period since the initialization (i.e.,  $k$  going from 0 to 10), which implicitly assumed the stationarity of the diffusivities over this timescale.

### 3 Results

#### a. Horizontal Diffusivities

Applying this methodology to compute the diffusivities ( $\kappa_{xx}$ ,  $\kappa_{yy}$ , and  $\kappa_{xy}$ ) to a starting location at  $30^\circ\text{N}$ ,  $40^\circ\text{W}$  shows the horizontal spreading of the 100 pseudo-trajectories (Fig. 5a). This spreading is monotonous along the zonal and meridional directions (Fig. 5b and d, respectively), but not for the cross-direction (Fig. 5f). The best linear fit of the spread of variances and covariance, following (10), gives a zonal, meridional, and cross diffusivities of  $494 \text{ m}^2 \text{ s}^{-1}$ ,  $535 \text{ m}^2 \text{ s}^{-1}$ , and  $-37 \text{ m}^2 \text{ s}^{-1}$  (Fig. 5c, e, and g), respectively.

We now reproduce this computation systematically all over the globe with starting points every  $1^\circ \times 1^\circ$  to compute the zonal, meridional, and cross diffusivities everywhere (Fig. 6). The first striking result is the inhomogeneity of the zonal, meridional, and cross diffusivities, with high values in the western boundary currents, the equatorial band, and the Antarctic Circumpolar Current, which is confirmed by regional averages (Tab. 1). Except at the equator, zonal and meridional diffusivities look alike. Their patterns correspond to high values of a few thousands to up to a few  $10,000 \text{ m}^2 \text{ s}^{-1}$  along western boundaries and within mid-latitude large, coherent ocean currents (e.g., Antarctic Circumpolar Current, Gulf Stream, North Atlantic Current, Agulhas Current, Kuroshio, and Zapiola Gyre). The maxima occur for the zonal diffusivities within the Zapiola Gyre and within the Agulhas Current retroflexion, which reach up to  $40,000 \text{ m}^2 \text{ s}^{-1}$  and are also regions of turbulent velocity maxima (Fig. 2c and d). To a lesser degree the Kerguelen and Campbell plateaus appear to be two others locations of strong zonal diffusivity. These hot spots of zonal diffusivity are also hot spots for the meridional diffusivity, but with weaker values ( $\sim 10,000 \text{ m}^2 \text{ s}^{-1}$ ), except for the Campbell plateau which exhibits higher meridional diffusivity than zonal diffusivity. On the other hand, the diffusivities in the basin interior are much less with values of only a few hundred of  $\text{m}^2 \text{ s}^{-1}$  (Fig. 6a and b). Along the equator, meridional diffusivity is weak (from a few hundred to a thousand of  $\text{m}^2 \text{ s}^{-1}$ ) whereas zonal diffusivity is intense (several thousand of  $\text{m}^2 \text{ s}^{-1}$ ), consistently with low and high values of meridional and zonal turbulent velocities (Fig. 2c), respectively (the latter being due to the succession of zonal currents and counter-currents, as well as propagating equatorial waves). The high value of meridional diffusivity along Eastern Africa (Fig. 6b) is consistent with the local maximum of meridional turbulent velocity (Fig. 2d), imprinted by the Somali Current intermittent behaviour. Overall the zonal and meridional diffusivities show intensification in regions which have a high level of turbulent activity (Fig. 2c and d, also see section 3b. for further investigations on that). The cross diffusivity shows positive values of up to  $10,000 \text{ m}^2 \text{ s}^{-1}$  along the western boundaries,

whereas negative values of down to  $-10,000 \text{ m}^2 \text{ s}^{-1}$  occur in most place along the Antarctic Circumpolar Current (Fig. 6c). The global mean values of the zonal, meridional, and cross diffusivities are  $1,324 \text{ m}^2 \text{ s}^{-1}$ ,  $969 \text{ m}^2 \text{ s}^{-1}$ , and  $-8 \text{ m}^2 \text{ s}^{-1}$  (Fig. 6).

To test the robustness of our results, we have computed the accuracy of the linear regression between the time evolution of the (co-)dispersion and time. For the zonal and meridional directions the fit is extremely accurate, with error of a few percents (estimated as the residual of explained variance) in most of the regions, reaching values, at worst, ranging from 10 to 20% in a few specific locations (Fig. 7a and b). For the cross direction, the error is one order of magnitude above, with error that can often reach 100% (Fig. 7c). This is consistent with the analysis located at  $30^\circ\text{N}$ ,  $40^\circ\text{W}$  (Fig. 5). However, this error is weaker in region of intense cross diffusivities (often less than 20%). This means that the fit is less accurate where the cross-diffusivities is weak anyway. The scatterness of the local error in those regions, suggests that large-scale consistency of the cross-diffusivities (as the overall weak values in the basin interior) is probably still accurate.

To quantify the variations of zonal, meridional, and cross diffusivities, we compute histogram of their spatial-density distribution (using uniform  $50 \text{ m}^2 \text{ s}^{-1}$  bins, Fig 8). We find that the zonal and meridional distributions have a significant skewness toward high diffusivity values. Consistently with this type of distributions, we see that, for both zonal and meridional diffusivities, the most common value (i.e., the mode) is lower than the most typical value (i.e., the median) which is lower than the expected value (i.e., the mean). Thus, we find a most common value of  $250 \text{ m}^2 \text{ s}^{-1}$  and of  $250 \text{ m}^2 \text{ s}^{-1}$ , a most typical value of  $650 \text{ m}^2 \text{ s}^{-1}$  and of  $450 \text{ m}^2 \text{ s}^{-1}$ , and an expected value of  $1,324 \text{ m}^2 \text{ s}^{-1}$  and of  $969 \text{ m}^2 \text{ s}^{-1}$  for the zonal and meridional diffusivities, respectively. It is interesting to note that for these two distributions, despite most values are restricted to weak diffusivities (below  $1,000 \text{ m}^2 \text{ s}^{-1}$ ), extreme values (of several  $1,000 \text{ m}^2 \text{ s}^{-1}$  or above) still occur.

For the cross diffusivities the distribution follow a bell curve with a most common value

of  $-50 \text{ m}^2 \text{ s}^{-1}$  (closely followed by  $+50 \text{ m}^2 \text{ s}^{-1}$ ), a most typical value of  $-25 \text{ m}^2 \text{ s}^{-1}$ , and an expected value of  $-8 \text{ m}^2 \text{ s}^{-1}$ . Overall, this suggests that it is a symmetric distribution centered around 0. As for the zonal and meridional diffusivity distributions, extreme values reach beyond  $\pm 1,000 \text{ m}^2 \text{ s}^{-1}$ , despite most of the values remain within a few  $\pm 100 \text{ m}^2 \text{ s}^{-1}$ . Beyond the quantitative values, the cross-diffusivity is also indicative of the diffusion acting along directions that are not co-aligned with the longitudes and latitudes (e.g., Rypina et al., 2012). This property is especially visible in region of strong diffusivity (where the cross-diffusivity is also important). To investigate the properties of the diffusivity tensor, we compute its eigenvectors and eigenvalues. The eigenvectors give the natural directions of diffusivity, whereas the eigenvalues give the diffusivity coefficient acting along these directions. Hence the diagonalization of  $\mathbf{K}$  reads:

$$\mathbf{K} = \begin{pmatrix} \kappa_{xx} & \kappa_{xy} \\ \kappa_{xy} & \kappa_{yy} \end{pmatrix} = \begin{pmatrix} p_x & s_x \\ p_y & s_y \end{pmatrix} \begin{pmatrix} \kappa_p & 0 \\ 0 & \kappa_s \end{pmatrix} \begin{pmatrix} p_x & p_y \\ s_x & s_y \end{pmatrix}, \quad (11)$$

where  $\kappa_p$  and  $\kappa_s$  are the primary and secondary diffusivities acting along the horizontal directions defined by  $(p_x, p_y)$  and  $(s_x, s_y)$ , respectively,  $p_x$  and  $p_y$  are the zonal and meridional vector coordinates of the primary diffusivity direction, respectively, and  $s_x$  and  $s_y$  are the zonal and meridional vector coordinates of the secondary diffusivity direction, respectively. These vectors are normalized such as  $p_x^2 + p_y^2 = s_x^2 + s_y^2 = 1$ . Because  $\mathbf{K}$  is represented by a symmetric matrix (normal operator), its eigenvectors are orthogonal ( $p_x s_x + p_y s_y = 0$ ). The primary and secondary diffusivities act orthogonally to each other.

This diagnostic reveals that there is indeed a primary direction for diffusivity (Fig. 9). The global average along this primary direction reaches  $1,672 \text{ m}^2 \text{ s}^{-1}$ , whereas the global diffusivity acting along the secondary direction is only  $621 \text{ m}^2 \text{ s}^{-1}$  (Tab. 1). This means that the diffusivity is almost 3 times as strong along its primary direction as along its secondary one, whereas it was quite well balanced when measured along the zonal and meridional directions (albeit a slight dominance of zonal over meridional diffusivity). This property

is also visible for regional averaged values (Tab 1). As expected, the primary (as well as, by construction, the secondary) direction varies significantly spatially. Within the gyre interior, the weak difference between diffusivities acting along the primary and secondary direction, as well as the lack of consistency of the natural directions, suggests the isotropy of diffusivity (Fig. 10a, this was also the region where the cross-diffusivity was weak, Fig. 6c). On the other hand, this rotated framework shows regions with strong diffusivity and coherent natural directions for diffusivities. For instance, the equatorial region as a well coherent primary direction along the zonal direction (and a meridional secondary direction). Southern Ocean, western boundary currents, and gyre recirculations also exhibit organized primary direction (Fig. 9). In these regions, since the primary and secondary natural direction are not aligned with zonal and meridional directions, this allows for a better amplitude separation between the primary and secondary diffusivities (vs zonal and meridional diffusivities). This leads, for instance, to values of up to  $74,000 \text{ m}^2 \text{ s}^{-1}$  along the primary direction within the Agulhas current retroflection and within the Zapiola gyre (Fig. 9), whereas it remains below  $4,000 \text{ m}^2 \text{ s}^{-1}$  along the secondary direction at the same locations (which corresponds to almost a factor 20 between the two directions). Regions with strong difference in primary and secondary diffusivities correspond to regions of strong diffusivity anisotropy (Fig. 10a). We could cite the equator, the western boundary currents, and the Antarctic Circumpolar Current. On the other hand, regions away from the coast, and in particular away from the western boundary currents, and gyre interiors appear to experience an isotropic diffusivity.

To test the sensitivity to the resolution, we have carried out this full analysis with a lower resolution of  $5^\circ \times 5^\circ$  (instead of  $3^\circ \times 3^\circ$ ) to compute the statistical properties of the analog trajectories (as described in section 2b.). The area distributions of the zonal, meridional, and cross diffusivities for the  $5^\circ \times 5^\circ$  resolution have a similar shape than the ones for the  $3^\circ \times 3^\circ$  resolution (Fig. 8). The most common value (mode), the most typical value (median), and the expected value (mean) of the distributions remain also similar. The main difference

is a slight tightening of the distribution that reduces the occurrence of extreme values at the advantage of more typical ones. This is consistent with the smoothing or averaging properties expected from the use of a larger resolution.

*b. Diffusivity Scalings*

As mentioned previously, there is a degree of agreement between the regions of enhanced turbulent activity and the patterns of intense zonal and meridional diffusivities, such as the Antarctic Circumpolar Current, the Zapiola Gyre, the Agulhas Current retroflection, and the equatorial region. Hence, we further investigate this relationship. To this purpose, we can scale the zonal, meridional, and cross diffusivities with the zonal and meridional turbulent velocities, and the covariance velocities (Fig. 2c and d) computed in (2).

We test two classical turbulent scalings relating the diffusivities to either the turbulent velocities or their squared value (Vallis, 2006). The scaling of diffusivity with turbulent velocities predicts a length scale, whereas the scaling of diffusivity with the velocity variance predicts a time scale. Hence we diagnose the turbulent length and time scales, such as:

$$\kappa_{xx} = \tilde{u} l_{\text{turb}}^x, \quad (12a)$$

$$\kappa_{yy} = \tilde{v} l_{\text{turb}}^y, \quad (12b)$$

and

$$\kappa_{xx} = \tilde{u}^2 t_{\text{turb}}^{xx}, \quad (13a)$$

$$\kappa_{yy} = \tilde{v}^2 t_{\text{turb}}^{yy}, \quad (13b)$$

$$\kappa_{xy} = \tilde{c}^2 t_{\text{turb}}^{xy}, \quad (13c)$$

where  $l_{\text{turb}}^{\{x,y\}}$  are zonal and meridional turbulent length scales, respectively, effectively a mixing length; and  $t_{\text{turb}}^{\{xx,yy,xy\}}$  are the zonal, meridional, and cross turbulent time scales, respectively, which is effectively the Lagrangian integral time scale (Taylor, 1921; Riser and Rossby, 1983).

It worth noting that a range of studies have described the effect of mean flow acting to suppressed the cross (i.e., orthogonal to the mean flow) term mixing (Ferrari and Nikurashin, 2010; Klocker et al., 2012). Similarly the mixing has been suggested to be enhanced along the mean flow (Nummelin et al., 2021). In these contexts, the closures suggested above would need to be modified to account for that. However, in our study we have avoided this difficulty by suppressing the action of the mean flow [cf. (3)]. Hence, we kept the more classical closure schemes described in (12) and (13), consistently with pioneering studies of Prandtl (1925) and Taylor (1921), respectively. The main hypothesis of these studies is the homogeneity, which is assumed to hold locally in our study.

It appears that the turbulent length scales still show a lot of large scale structures that could be associated to gyres or coherent currents (Fig. 11). Indeed the turbulent length scales decrease inside gyres and increase in the equatorial region, in western boundary currents, and in locations of intense circulations, such as in the North Atlantic with the North Atlantic Current or in the Southern Ocean with the Antarctic Circumpolar Current. This is confirmed by regional averages (Tab. 1). Unlike previously suggested (e.g., Ollitrault and Colin de Verdière, 2002), in our study the turbulent length scales do not scale with the Rossby deformation radius. On the other hand, the turbulent time scales associated with the zonal and meridional directions do not show large scale structure and are overall quite constant (Fig. 12a and b, respectively). This suggests that a time scale is a better scaling factor than length scale, and that (13) appears more valid than (12) to extract the essence of the zonal and meridional diffusivity coefficients.

This result is further confirmed by comparing the linear relationship between the diffusivities and the turbulent velocities or the squared turbulent velocities (Fig. 13). This last analysis suggests that, despite a broad degree of uncertainty, the quadratic scaling from (13) is more robust than the linear one from (12), with a percentage of variance explained by the time scale closure of 62% and 56% for the zonal and meridional diffusivities, falling to only

49% and 53%, respectively, for the length scale closure.

Regarding the cross diffusivities, we can apply the same scaling principle to find the cross turbulent length scale (13c). The uncertainty appears larger than for the zonal and meridional directions. Cross turbulent time scale shows large variations and no clear patterns (Fig. 12c), whereas the best linear fit (Fig. 13e) explains only 12% of the relationship between cross diffusivities ( $\kappa_{xy}$ ) and the covariance velocities ( $\tilde{c}^2$ ).

Despite variable in space, we can build an area distribution of the turbulent length and time scales to see if any prevalent values emerge (Fig. 14). The turbulent length scale is strongly varying with a most common values in the range between 10-12 km, for both zonal and meridional directions (Fig. 14a). Given the skewness of the distributions, the expected values (24 and 19 km, respectively) are different and larger than the most common values. The inconsistency of these most common values with the linear fit between diffusivities and velocities (37 km and 30 km for zonal and meridional directions, respectively, Fig. 13) further suggests the inaccuracy of the turbulent closure through the turbulent length scale described in (12). On the other hand, the area distribution of the turbulent time scales is sharper with a relatively lower standard deviation and skewness (Fig. 14b). The most common values are 4.5-5 days, for both zonal and meridional directions. This is consistent with the best linear fit between diffusivities and turbulent velocity variances of 5.3 days and 4.5 days for zonal and meridional velocities (Fig. 13), respectively. This overall consistency and the tighter area distribution suggest the usefulness of the time scale closure for turbulent diffusivities described in (13). It is worth noting that there still exists potentially significant variations of the regionally averaged turbulent time scales (Tab .1), with values reaching almost the year in the subtropical North Pacific interior and the Southern Ocean. For the cross diffusivity, the most common value is 2-4 days (Fig. 14c). Despite the consistency with 3.7 days found for the best linear fit (Fig. 13e), the cross turbulent time scale is not as robust as the zonal and meridional turbulent time scales because of the large spread of the distribution

(Fig. 14c). This spatial area distribution analysis confirms the result of the previous analysis on the geographic distribution of the turbulent length and time scales and on the prevailing accuracy of the turbulent time scale closure over the turbulent length scale closure.

To further test the relationship between the turbulent flow and the diffusivity, we check if the natural diffusivity directions (i.e., eigenvectors of the diffusivity operator) are consistent with the natural directions of the turbulent velocity variance [consistently with the closure of (13)]. These latter natural directions are computed as the eigenvectors of the turbulent velocity covariance matrix ( $\Sigma$ ) and are the Empirical Orthogonal Functions (EOFs) of the local turbulent velocity. This decomposition reads:

$$\Sigma = \begin{pmatrix} \tilde{u}^2 & \tilde{c}^2 \\ \tilde{c}^2 & \tilde{v}^2 \end{pmatrix} = \begin{pmatrix} \tilde{p}_x & \tilde{s}_x \\ \tilde{p}_y & \tilde{s}_y \end{pmatrix} \begin{pmatrix} \tilde{u}_p^2 & 0 \\ 0 & \tilde{u}_s^2 \end{pmatrix} \begin{pmatrix} \tilde{p}_x & \tilde{p}_y \\ \tilde{s}_x & \tilde{s}_y \end{pmatrix}, \quad (14)$$

where  $\tilde{u}_p^2$  and  $\tilde{u}_s^2$  are the primary and secondary turbulent velocity variance acting along the horizontal directions defined by  $(\tilde{p}_x, \tilde{p}_y)$  and  $(\tilde{s}_x, \tilde{s}_y)$ , respectively,  $\tilde{p}_x$  and  $\tilde{p}_y$  are the zonal and meridional vector coordinates of the primary turbulent velocity variance direction, respectively, and  $\tilde{s}_x$  and  $\tilde{s}_y$  are the zonal and meridional vector coordinates of the secondary turbulent velocity variance direction, respectively. These vectors are normalized such as  $\tilde{p}_x^2 + \tilde{p}_y^2 = \tilde{s}_x^2 + \tilde{s}_y^2 = 1$ . As for  $\mathbf{K}$ ,  $\Sigma$  being a symmetric matrix (normal operator), its eigenvalues are orthogonal ( $\tilde{p}_x \tilde{s}_x + \tilde{p}_y \tilde{s}_y = 0$ ), so that the primary and secondary turbulent velocity variances act orthogonally to each other. This property is quite useful to compare the directions of the turbulent flow and of the diffusivity, since comparing their primary direction, is also, virtually, comparing their secondary direction. Finally, it is interesting to note that Eddy Kinetic Energy remains conserved through the rotation of the coordinates from zonal-meridional to EOFs, since the trace of the matrix is constant ( $\tilde{u}^2 + \tilde{v}^2$  and  $\tilde{u}_p^2 + \tilde{u}_s^2$ , respectively). Hence to set the quantitative comparison between natural direction of diffusivity and of the turbulent flow, we define the angle from the north as  $\theta = \arctan(p_x/p_y)$  and  $\tilde{\theta} = \arctan(\tilde{p}_x/\tilde{p}_y)$  for the primary diffusivity direction and for the primary turbulent velocity

variance direction, respectively. To further test the impact of the flow dynamics on the diffusivity we also defined the mean flow direction as:  $\bar{\theta} = \arctan(\bar{u}/\bar{v})$ .

To test the relation between  $\theta$  and  $\tilde{\theta}$  or  $\bar{\theta}$ , we plot them against each other (Fig 10b or c, respectively). This reveals that indeed, despite a degree of uncertainty, a one-to-one relation exists between the natural diffusivity directions and the natural turbulent flow direction (Fig 10b). On the other hand, there is no obvious relationship between the primary diffusivity direction and the mean flow direction (Fig 10c). This differs from the widely used hypothesis stating that the mean flow enhances and suppresses the diffusivity along and across its direction, respectively (Ferrari and Nikurashin, 2010; Klocker and Abernathey, 2014; Groeskamp et al., 2020; Nummelin et al., 2021). However, we remind the reader that we have removed the effect of the mean advection in (3), which could explain this apparent disagreement. Hence, we conclude that the natural diffusivity direction is set by the natural direction of the turbulent flow (i.e., Eddy Kinetic Energy or variance of the velocities). Note that testing the relationship by only keeping region of high diffusivities, where the diffusivity directions are well organized, does not improve the relationships.

#### 4 Discussions and Conclusions

The observed ocean circulation is the result of the action of several physical processes and their interactions. One of this process is turbulent mixing quantified by the horizontal diffusion. It is crucial for the ocean circulation from local to global scale, as well as for water mass transformation and ventilation (Abernathey and Ferreira, 2015). Diffusion is not only important for the physical properties of the ocean, but also for carbon and nutrient distribution and evolution, especially in region of intense eddy activity (Wunsch, 1999).

In this study we have computed the horizontal diffusivity coefficients of the ocean at  $\sim 1,000$  m depth from observed Lagrangian displacements. These observations are recorded by Argo floats through their 10-day journey at parking depth and gathered and validated in

the ANDRO dataset (Ollitrault et al., 2019). Because they are the cycling between surface drift and transmission, drift at parking depth, and water column profiling, the Argo floats do not provide continuous trajectories. Furthermore, the initial position of Argo floats are not co-located. These discontinuity and initial position issues must be cared for to discuss the spreading as actual Lagrangian floats over a few months. To do so, we have reconstructed likely pseudo-trajectories, which are continuous in time and in agreement with the statistical properties of the Argo float displacements at depth. This has been done using an analog method, whose efficiency has been demonstrated in a range of previous studies (e.g., Ayet and Tandeo, 2018; Sévellec and Drijfhout, 2018).

Using this method, we obtain the dispersion of pseudo Lagrangian particles and can infer the diffusivity coefficients along the zonal, meridional, and cross directions. This analysis reveals that the diffusion is anisotropic and that the diffusivity coefficients are highly varying in space. We find values ranging from a few  $100 \text{ m}^2 \text{ s}^{-1}$  in the ocean interior to several  $1,000 \text{ m}^2 \text{ s}^{-1}$  in western boundary currents or along the Antarctic Circumpolar Current, up to several  $10,000 \text{ m}^2 \text{ s}^{-1}$  in a few specific hot spots (Zapiola gyre and Agulhas Current retroflection). For the zonal diffusivity coefficient, values ranging from several  $1,000 \text{ m}^2 \text{ s}^{-1}$  to a few  $10,000 \text{ m}^2 \text{ s}^{-1}$  are also found at and in the vicinity of the equator. Overall the global mean zonal diffusivity coefficient reached  $1,324 \text{ m}^2 \text{ s}^{-1}$ , where it is slightly below  $1,000 \text{ m}^2 \text{ s}^{-1}$  for the meridional diffusivity. In comparison the cross-diffusivity averages out, and reached values of  $10,000 \text{ m}^2 \text{ s}^{-1}$  within intense boundary currents and in the Southern Ocean.

To further characterize the diffusivity coefficients, we have tested two empirical closures: one relates the coefficients to the local turbulent velocities and the other to variance of the local velocities (the latter being the square of the former). Linear regression allows us to compute the turbulent length and time scale, respectively. We find that the zonal and meridional turbulent length scales have a globally average values of 24 and 19 km, but vary quite significantly spatially. These variations bear a resemblance with the turbulent velocities

(i.e., intensification along western boundary, in the Southern Ocean, and at the equator). On the other hand, we find that the zonal and meridional turbulent time scales show quite spatially-uniform values with a most common value of 4.5-5 days. The nearly spatially-constant turbulent time scale is particularly striking given the huge spatial variations of the diffusivity coefficients. This suggests that the Eddy Kinetic Energy captures well the spatial variations of the diffusivity coefficients at this 1,000-m depth. From this analysis, we conclude that the turbulent velocity variance closure is favored, leading to an almost universal turbulent time scale of 4.5-5 days.

In this study, we have also taken advantage of the computation of the cross diffusivity coefficient to rotate the diffusivity along its natural directions. This rotation is not important within the ocean interior (where diffusivity is mainly isotropic) but is more crucial along western boundaries and in the Southern Ocean. Within this new framework, the diffusivity coefficient reached up to  $74,000 \text{ m}^2 \text{ s}^{-1}$  (in the Zapiola gyre and in the Agulhas Current retroflection). This increase of diffusivity coefficients is expected, since the rotation boosts the diffusivity along the primary direction (and decreases it along the secondary direction) when compared to values along the zonal and meridional directions (and further demonstrate the anisotropy of the diffusion). This property is a natural outcome of the conservation of the trace of the diffusivity operator, which follows the rotational invariance of Eddy Kinetic Energy, given the accuracy of the turbulent time scale closure discussed in the paragraph above. We also show that primary direction is well aligned, with a degree of uncertainty, to the primary direction of horizontal velocity variance, but is not particularly aligned to the direction of the mean flow.

There has been a range of local eddy resolving *in situ* experiments in the North Atlantic from which the horizontal diffusivity coefficients have been estimated. Using SOFAR floats (Lagrangian floats positioned by acoustic), Freeland et al. (1975) in the Mode region found  $\kappa_{yy}=710 \text{ m}^2 \text{ s}^{-1}$  around  $28^\circ\text{N}$ ,  $69^\circ\text{W}$  at 1,500 m depth. Riser and Rossby (1983) measured

diffusivity coefficients of  $\kappa_{xx}=4,500 \text{ m}^2 \text{ s}^{-1}$  and  $\kappa_{yy}=1,800 \text{ m}^2 \text{ s}^{-1}$  (with  $\pm 50\%$  uncertainties) at 700-m depth and within the 25-30°N and 67-75°W region. Böning (1988) reported unpublished values from Price (also reported in Rossby et al., 1983) of  $\kappa_{xx}=1,500\pm 1,000 \text{ m}^2 \text{ s}^{-1}$  and  $\kappa_{yy}=1,500\pm 500 \text{ m}^2 \text{ s}^{-1}$  at 1,300 m depth from the Local Dynamics experiment in the North Atlantic. All these reported values are in the range of our own estimations for the region, validating, *a posteriori*, our study and inherent assumptions. At the same location and 700-m depth, Ollitrault and Colin de Verdière (2002) showed an interesting property of the diffusivity, whereas west of the Mid-Atlantic ridge they reported values of  $5,000 \text{ m}^2 \text{ s}^{-1}$ , east of the Mid-Atlantic Ridge they found values of only  $2,200 \text{ m}^2 \text{ s}^{-1}$ . This spatial variation is qualitatively and quantitatively consistent with our analysis that reveals changes in the diffusivity coefficients between region of active turbulence (e.g., west of the Mid-Atlantic Ridge) and the more laminar ocean gyre interior (e.g., east of the Mid-Atlantic Ridge). Alternative methods diagnosing diffusivity through turbulent advection, either along the 27.9  $\text{kg m}^{-3}$  isopycnal (Chapman and Sallée, 2017) or for full ocean depth (Groeskamp et al., 2020), show at  $\sim 1,000$ -m depth consistent values to our estimates.

More recently, a dedicated experiment using both passive tracer and Lagrangian acoustically-positioned floats was achieved under the Diapycnal and Isopycnal Mixing Experiment in the Southern Ocean (DIMES, Naveira Garabato, 2010; Meredith, 2011). The release of passive tracer and floats was located at 57°S, 105°W, east of the Drake Passage. The two methods found a meridional (cross-mean flow) diffusivity of  $710\pm 260 \text{ m}^2 \text{ s}^{-1}$  (at 1,500-m depth, Tulloch et al., 2014) and  $800\pm 200 \text{ m}^2 \text{ s}^{-1}$  (at 950-m depth, LaCasce et al., 2014), respectively. To quantitatively test our method, we have reproduced this analysis by initializing the pseudo-trajectories at the location of DIMES tracer and float releases. To make the comparison more accurate, we have aligned our estimation protocol with the one of LaCasce et al. (2014) and Tulloch et al. (2014). Hence, we have removed the constrain on the mean flow [i.e., allowing mean advection by removing the last term in the right handside of (3b)] and

computed the diffusivity coefficient over 1 year. We obtain  $\sim 950 \text{ m}^2 \text{ s}^{-1}$  for the meridional diffusivity coefficient at 1,000-m depth, which confirms the quantitative skill of our method (i.e., trajectory reconstruction by the analog method). However, we argue that these two previous studies suffer from inherent methodological limitations. First, three months is more appropriate than one year to sample the turbulent diffusive regime. Indeed computation over too long timescales underestimates the diffusivity (because the tracer variance increase is partially computed over the saturated regime). The decrease of cross-diffusivity with longer integration time scale have also been reported by Zhurbas et al. (2014) in the context of surface drifters. Secondly, because the estimation is done along the mean flow pathways (which is significant in the region), it is not a local estimate but it represents an integral along the pathway (which is long for a 1-year estimation). Since we can correct for both limitations in our setting, we obtain instead:

- $\sim 1,575 \text{ m}^2 \text{ s}^{-1}$ , for estimation over 100 days, and
- $\sim 1,570 \text{ m}^2 \text{ s}^{-1}$ , for estimation over 100 days and with removing the ensemble mean advection.

Hence, we consider the last value to be the more accurate estimation at that location. [Note that removing the mean flow affects particularly the along-mean flow estimation (zonal direction at DIMES location), which was not discussed in Tulloch et al. (2014) and LaCasce et al. (2014)]. It is a demonstration or confirmation, if needed, that the diffusivity coefficients computed along a path [Lagrangian view:  $\tilde{\kappa}(x(t), y(t))$ ] or at a fixed point [Eulerian view:  $\kappa(x, y)$ ] can differ by more than 50% because of the high spatial variability of the coefficient. This argument highlights the difficulty of the comparisons between the two estimations.

There also exists global studies of estimation of the lateral diffusivity coefficients. For instance, Cole et al. (2015) found values from only a few  $100 \text{ m}^2 \text{ s}^{-1}$  (subpolar gyre interior) to several  $10,000 \text{ m}^2 \text{ s}^{-1}$  (western boundary currents) at the base of the mixed layer (described

at  $\sim 100$ -m depth, except in high latitudes where it reaches a few 100-m depth). Once again this study is qualitatively consistent with our results (i.e., spatial variation of the diffusivity with intensification near intense boundary currents), however the difference in depth location (mixed-layer vs intermediate depth) prevents us from further quantitative comparisons. Maybe the most straightforward comparison is with the results of Roach et al. (2018). Although they use the same observations (Argo deep displacements), their method and related assumptions completely differ from ours. They reported cross-mean-flow diffusivity of  $543 \pm 155 \text{ m}^2 \text{ s}^{-1}$  in agreement with our estimations, with spatial variation comparable to our secondary-direction diffusivity.

Beyond the purely quantitative estimation of the diffusivity coefficients, we have also shown that the diffusivity scales best with the turbulent velocity variance (vs its standard deviation, as sometime hypothesized), a result consistent with Taylor (1921). In our analysis we found that the closure is especially robust in homogeneous and isotropic regions (i.e., ocean gyre interior), assumptions at the base of Taylor's results (1921). Beyond the usefulness of the closure with the turbulent velocity variance, we show that the covariance function time integral (leading to the Lagrangian integral time scale) is mainly spatially uniform with a value of 4.5-5 days (despite it is more accurately described as a distribution). This universal time scale contrasts with the high resolution model estimations of the Lagrangian integral time scale by Griesel et al. (2010), which was found to be highly spatially varying. However values from other regional observational studies are consistent with ours. Hence, Lumpkin et al. (2002) found a spatially uniform Lagrangian timescale of  $\sim 6$  days at 700-2,000 m depth in the mid-latitudes of the North Atlantic. In the same region, Ollitrault et al. (2005) suggested a Lagrangian integral time scale of 7-10 days and 5-6 days at the west and the east of the mid-Atlantic ridge, respectively. These two values are quite close (and notably consistent with our estimates of  $\sim 7$  and  $\sim 5$  days for these regions, ST-NA-WB and ST-NA-I in Tab 1, respectively), despite the wide difference in the Eddy Kinetic Energy

between the west and the east (pleading in favor of a universal time scale). In the Mode region, Riser and Rossby (1983) reported values between 7 to 18 days, whereas (Freeland et al., 1975) reported values between 10 and 12 days. Despite being in the upper range of our estimation distribution (Fig. 14b), these values remain within our local and regional estimations (Fig. 12a, b and Tab 1, respectively). Also, both studies suggest the spatial anisotropy of the Lagrangian integral time scales in the studied region. This is consistent with our local and regional estimations showing that boundary regions are where the universality of the Lagrangian integral time scale breakdown (Fig. 12a, b and Tab 1).

We have seen that our diffusivity estimates do not exhibit a suppressed direction across the direction of the mean flow, as suggested by Ferrari and Nikurashin (2010), Klocker and Abernathey (2014), and Groeskamp et al. (2020). At the opposite we find that the natural directions of the diffusivity have no distinct relationship with the direction of the mean flow. This could be linked to the diffusivity estimation method used in our study, which deliberately removes the direct action of the mean flow on Lagrangian tracer ensemble (albeit, the turbulence is still derived from a circulation where the mean flow exists). Alternatively, this could be linked to the isotropic diffusivity assumption at the heart of the enhanced and suppressed diffusivity hypothesis (Nummelin et al., 2021). Indeed, we have shown that the diffusivity coefficients in the absence of mean flow are strongly anisotropic following the natural directions of the horizontal velocity variance. Hence, it is possible that the suppressing and enhancing effects are second order effects of an anisotropic diffusion. In particular, our closures fully acknowledged both directions independently (13), unlike the one suggested by Ferrari and Nikurashin (2010) and Groeskamp et al. (2020), for instance, where a single measure of turbulent velocities (i.e.,  $\sqrt{\tilde{u}^2 + \tilde{v}^2}$ ) is used. However, our closures exhibit zonal and meridional turbulent time scale longer and shorter than average, respectively, in the Gulf Stream and in part of the Antarctic Circumpolar Current (Fig. 12a and b). Hence rationalizing the role of the mean flow in an anisotropic turbulent field will be the subject

of a follow up study.

Let us now list the shortcomings of our study. The primary one is the discontinuity of the Argo float displacements. Hence, and despite having been fully assessed in our study, the assumptions behind the analog method used to reconstruct pseudo-trajectories remain a source of uncertainties and errors. In particular this ignore the motions above the Nyquist frequency of  $\sim 1/20$  cycles per day. Also it would be interesting to test more sophisticated method based on more advanced artificial intelligence procedure, such as deep learning, for comparison and to test the robustness of the results. In particular, we would like to account for the memory of the Lagrangian trajectories (e.g., Berloff and McWilliams, 2002) and to acknowledge non-normal displacement distribution related to extreme events (e.g., Bracco et al., 2000). Another difficulty is that, by design of the Argo float/network, the displacement observations are only made at a single depth level (1,000 m). This does not allow the computation of the horizontal diffusivity coefficients for the full 3D ocean and to track how they change with depth. Other methodologies would be needed for this purpose.

The current study and developed methodology offer a range of future applications. For instance, focusing at the surface, flotsam dispersion can be estimated using surface drifters (which are not discontinuous, but are not co-located), with natural implication for ocean plastic pollution. It would be particularly interesting to investigate the role of new physical mechanisms at play at the surface, such as Ekman transport or surface-wave Stokes drift, and to determine their respective impact on the dispersion. More generally our study and the estimation of diffusivity coefficients can be used for parameterization of passive tracer diffusion in eddy-less model (simply following  $\mathbf{K} \simeq \Sigma \times 5$  days, which can be estimated from direct observations of Eddy Kinetic Energy, similar to the suggestion of Holloway, 1986). Following the same logic, these coefficients can be used as a benchmark to validate eddy-permitting and eddy-resolving ocean models. When these models will be able to reproduce surface and 1,000-m depth dispersion they will become useful to estimate the vertical variations of the

diffusion coefficients. All these will be directions for future work.

*Acknowledgment.* This research was supported by the OceaniX project funded through the French ANR program and by the ISblue project, Interdisciplinary graduate school for the blue planet (ANR-17-EURE-0015) and co-funded by a grant from the French government under the program “Investissements d’Avenir”. The ANDRO dataset used in this study corresponds to the 2019 Release (key: 66657) and is freely available through the [www.seanoe.org](http://www.seanoe.org) platform (<https://doi.org/10.17882/47077>).

## References

- Abernathy, R. and D. Ferreira, 2015: Southern Ocean isopycnal mixing and ventilation changes driven by winds. *Geophys. Res. Lett.*, **42**, 10 357–10 365.
- Ayet, A. and P. Tandeo, 2018: Nowcasting solar irradiance using an analog method and geostationary satellite images. *Solar Energy*, **164**, 301–315.
- Balwada, D., et al., 2021: Relative Dispersion in the Antarctic Circumpolar Current. *J. Phys. Oceanogr.*, **51**, 553–574.
- Batchelor, G. K., 1949: Diffusion in a field of homogeneous turbulence. *Australian Journal of Scientific Research*, **2**, 437–450.
- Berloff, P. S. and J. C. McWilliams, 2002: Material transport in oceanic gyres. Part II: Hierarchy of stochastic models. *J. Phys. Oceanogr.*, **32**, 797–830.
- Böning, C. W., 1988: Characteristics of particle dispersion in the North Atlantic: an alternative interpretation of SOFAR float results. *Deep-Sea Res.*, **35**, 1379–1385.
- Bracco, A., J. H. LaCasce, and A. Provenzale, 2000: Velocity probability density functions for oceanic floats. *J. Phys. Oceanogr.*, **30**, 461–474.
- Capet, X., et al., 2013: Eddies in Eastern Boundary Subtropical Upwelling Systems. *In Ocean Modeling in an Eddying Regime*, 131–147.
- Chapman, C. and J.-B. Sallée, 2017: Isopycnal Mixing Suppression by the Antarctic Circumpolar Current and the Southern Ocean Meridional Overturning Circulation. *J. Phys. Oceanogr.*, **47**, 2023–2045.
- Chen, R., et al., 2015: A Multiwavenumber Theory for Eddy Diffusivities and Its Application to the Southeast Pacific (DIMES) Region. *J. Phys. Oceanogr.*, **44**, 1877–1896.

- Cole, S. T., et al., 2015: Eddy stirring and horizontal diffusivity from Argo float observations: Geographic and depth variability. *Geophys. Res. Lett.*, **42**, 3989–3997.
- Colin de Verdière, A., T. Meunier, and M. Ollitrault, 2019: Meridional overturning and heat transport from Argo floats displacements and the planetary geostrophic method : applications to the subpolar North Atlantic. *J. Geophys. Res.*, **124**, 6270–6285.
- Colin de Verdière, A. and M. Ollitrault, 2016: Direct Determination of the World Ocean Barotropic Circulation. *J. Phys. Oceanogr.*, **46**, 255–273.
- Davis, R. E., 1987: Modeling eddy transport of passive tracers. *J. Mar. Res.*, **45**, 635–666.
- , 1991: Observing the general circulation with floats. *Deep-Sea Res.*, **38**, 531–571.
- de Lavergne, C., et al., 2016: The Impact of a Variable Mixing Efficiency on the Abyssal Overturning. *J. Phys. Oceanogr.*, **46**, 663–681.
- Delpech, A., et al., 2020: Deep eddy kinetic energy in the tropical Pacific from Lagrangian floats. *J. Geophys. Res.: Oceans*, **125**, e2020JC016313.
- Ferrari, R. and M. Nikurashin, 2010: Suppression of eddy diffusivity across jets in the Southern Ocean. *J. Phys. Oceanogr.*, **40**, 1501–1519.
- Freeland, H. J., R. P. and T. H. Rossby, 1975: Statistical observations of trajectories of neutrally buoyant floats in the North Atlantic. *J. Mar. Res.*, **33**, 383–404.
- Garrett, C., 2006: Turbulent dispersion in the ocean. *Prog. Oceanogr.*, **70**, 113–125.
- Griesel, A., et al., 2010: Isopycnal diffusivities in the Antarctic Circumpolar Current inferred from Lagrangian floats in an eddy model. *J. Geophys. Res.*, **115**, C06006.
- Groeskamp, S., et al., 2020: Full-depth global estimates of ocean mesoscale eddy mixing from observations and theory. *Geophys. Res. Lett.*, **47**, e2020GL089425.

- Holloway, G., 1986: Estimation of oceanic eddy transports from satellite altimetry. *Nature*, **323**, 243–244.
- Klocker, A. and R. Abernathey, 2014: Global Patterns of Mesoscale Eddy Properties and Diffusivities. *J. Phys. Oceanogr.*, **44**, 1030–1046.
- Klocker, A., et al., 2012: Reconciling float-based and tracer-based estimates of lateral diffusivities. *J. Mar. Res.*, **70**, 569–602.
- LaCasce, J. H., 2008: Lagrangian Statistics from Oceanic and Atmospheric Observations. *Lect. Notes Phys.*, **744**, 165–218.
- LaCasce, J. H., et al., 2014: Float-Derived Isopycnal Diffusivities in the DIMES Experiment. *J. Phys. Oceanogr.*, **44**, 764–780.
- Lumpkin, R., A.-M. Treguier, and K. Speer, 2002: Lagrangian Eddy Scales in the Northern Atlantic Ocean. *J. Phys. Oceanogr.*, **32**, 2425–2440.
- Meredith, M. P., 2011: Cruise report: RRS James Cook JC054 (DIMES UK2) 30 Nov 2010 to 8 Jan 2011. Tech. rep., British Antarctic Survey Cruise Rep. 206pp.
- Naveira Garabato, A. C., 2010: Cruise Report RRS James Cook JC041 (DIMES UK1) 5 Dec 2009 to 21 Dec 2009. Tech. rep., National Oceanography Centre Southampton Cruise Rep. 164pp.
- Nummelin, A., et al., 2021: Diagnosing the Scale- and Space-Dependent Horizontal Eddy Diffusivity at the Global Surface Ocean. *J. Phys. Oceanogr.*, **51**, 279–297.
- Ollitrault, M., C. Cabillet, and A. Colin de Verdière, 2005: Open ocean regimes of relative dispersion. *J. Mar. Res.*, **533**, 381–407.

- Ollitrault, M. and A. Colin de Verdière, 2002: Sofar floats reveal mid latitudes intermediate North Atlantic General circulation. Part II: an eulerian statistical view. *J. Phys. Oceanogr.*, **32**, 2034–2053.
- , 2014: The ocean general circulation near 1000-m depth. *J. Phys. Oceanogr.*, **44**, 384–409.
- Ollitrault, M. and J. P. Rannou, 2013: An Argo-based deep displacement dataset. *J. Atmos. Oceanic Technol.*, **30**, 759–788.
- Ollitrault, M., et al., 2019: ANDRO: An Argo-based deep displacement dataset. *SEANOE*, doi: 10.17882/47077.
- Pasquero, C., A. Provenzale, and A. Babiano, 2001: Parameterization of dispersion in two-dimensional turbulence. *J. Fluid Mech.*, **439**, 279–303.
- Portela, E., et al., 2020a: Interior water-mass variability in the southern hemisphere oceans during the last decade. *J. Phys. Oceanogr.*, **50**, 361–381.
- , 2020b: Physical mechanisms driving oxygen subduction in the global ocean. *Geophys. Res. Lett.*, **47**, e2020GL089040.
- Prandtl, L., 1925: Report on investigation of developed turbulence. Tech. rep., National Advisory Committee for Aeronautics.
- Riser, S. C. and H. T. Rossby, 1983: Quasi-Lagrangian structure and variability of the subtropical western North Atlantic circulation. *J. Mar. Res.*, **41**, 127–162.
- Roach, C. J., D. Bawada, and K. Speer, 2018: Global observations of horizontal mixing from Argo float and surface drifter trajectories. *J. Geophys. Res.: Oceans*, **123**, doi:10.1029/2018JC013750.

- Rossby, H. T., S. C. Riser, and A. J. Mariano, 1983: *The western North Atlantic—a Lagrangian viewpoint*. In: *Eddies in marine science*, A. R. Robinson, editor, Springer Verlag, Berlin, p. 609.
- Rypina, I. I., et al., 2012: Eddy-induced particle dispersion in the near-surface Atlantic. *J. Phys. Oceanogr.*, **42**, 2206–2228.
- Schott, F. A., S.-P. Xie, and J. P. McCreary Jr., 2009: Indian Ocean circulation and climate variability. *Rev. Geophys.*, **47**, RG1002.
- Sévellec, F., A. Colin de Verdière, and M. Ollitrault, 2017: Evolution of intermediate water masses based on Argo float displacement. *J. Phys. Oceanogr.*, **47**, 1569–1586.
- Sévellec, F. and S. S. Drijfhout, 2018: A Novel Probabilistic Forecast System Predicting Anomalously Warm 2018-2022 Reinforcing the Long-Term Global Warming Trend. *Nature Communications*, **3024**, 9.
- Taylor, G. I., 1921: Diffusion by continuous movements. *Proc. London Math. Soc.*, **20**, 196–212.
- Tulloch, R., et al., 2014: Direct Estimate of Lateral Eddy Diffusivity Upstream of Drake Passage. *J. Phys. Oceanogr.*, **44**, 2593–2616.
- Vallis, G. K., 2006: *Atmospheric and Oceanic Fluid Dynamics*. Cambridge University Press.
- van Sebille, E., et al., 2018: Lagrangian ocean analysis: Fundamentals and practices. *Ocean Modell.*, **121**, 49–75.
- Wang, T., et al., 2020: Eddy-induced acceleration of Argo floats. *J. Geophys. Res.: Oceans*, **125**, e2019JC016042.
- Wunsch, C., 1999: Where do ocean eddy heat fluxes matter? *J. Geophys. Res.*, **104**, 13,235–13,249.

- Wunsch, C. and R. Ferrari, 2018: One Hundred years of the Ocean General Circulation. *Meteorological Monographs*, **59**, 7.1–7.32.
- Ying, Y. K., J. R. Maddison, and J. Vanneste, 2019: Bayesian inference of ocean diffusivity from Lagrangian trajectory data. *Ocean Modell.*, **140**, 101–140.
- Zhurbas, V., D. Lyzhkov, and K. N., 2014: Drifter-derived estimates of lateral eddy diffusivity in the World Ocean with emphasis on the Indian Ocean and problems of parameterisation. *Deep-Sea Res.*, **83**, 1–11.
- Zika, J. D., et al., 2020: Tracking the spread of a passive tracer through Southern Ocean water masses. *Ocean Sci.*, **16**, 323–336.

## List of Figures

- 1 **Argo float deep displacement selection.** Distributions of (a) pressure and (b) period of Argo float deep displacements. Distributions are estimated from the entire ANDRO dataset (black) and after selecting displacements at a pressure between 950 and 1,150 dbar and with a period from 8.5 to 10.5 days (red). There are 1,041,054 displacements in the dataset and 675,575 displacements after selection. (c) Number of displacements from ANDRO dataset per  $3^\circ \times 3^\circ$  grid boxes for the selected 675,575 displacements (i.e., between 950 and 1,150 dbar and between 8.5 and 10.5 days). . . . . 43
- 2 **Mean and turbulent zonal and meridional velocities.** Colors show (a and b) zonal and meridional mean and (c and d) turbulent velocities ( $\text{cm s}^{-1}$ ), following (1) and (2), respectively. (d) Contours shows covariance of zonal and meridional velocities ( $\text{cm}^2 \text{s}^{-2}$ ), following (2). Velocities are computed each  $1^\circ \times 1^\circ$  as the velocity mean, standard deviation, and covariance within  $3^\circ \times 3^\circ$  grid boxes. Black, grey, and blue contours correspond to positive, zero, and negative values, with contour interval of  $20 \text{ cm}^2 \text{ s}^{-2}$ . (e) The red and black lines show the latitudes and longitudes separating the regions used in Tab. 1. The blue lines show the limits between western boundaries and interiors. . . 44
- 3 **Examples of 4 reconstructed pseudo-trajectories.** (a-d) The four continuous, likely trajectories are obtained using the analog method base on the ANDRO dataset (providing disconnected displacements from Argo floats during their journey at depth). They are initialized at  $30^\circ\text{N}$ ,  $40^\circ\text{W}$  and used a  $3^\circ \times 3^\circ$  grid to define the range of analogs. Crosses denote initial positions and lines denote displacements of both reconstructed continuous, likely trajectories (color) and observed disconnected Argo float displacements (grey). The color scale reflects the time evolution of the trajectories from 9.7 days to 97.4 days. . . . . 45
- 4 **Error estimation of the Gaussian fit approximation for the displacement probability density functions.** (a and b) Probability density function of longitudinal and latitudinal deep displacements (black bar), respectively, located at  $30^\circ\text{N}$ ,  $40^\circ\text{W}$ . (red crosses) The Gaussian fits are computed using the mean and the variance of the distribution displacement. To compute the error of the Gaussian fits, we compute the Missing Information (MI). The Missing Information measures the error of the fit by computing the ratio of the Kullback-Leibler divergence to the Shannon Entropy. (c and d) Maps of the error of the Gaussian fits for longitudinal and latitudinal displacements, respectively. . . . . 46

5	<p><b>Trajectory spread for initialization at 30°N, 40°W and computation of the diffusivity coefficients.</b> (a) 100 individual pseudo-trajectories (blue crosses – separating 10-day transition – linked by lines), their mean position (white cross) and their plus/minus zonal and meridional standard deviation (horizontal and vertical thick lines, respectively, with colorscale – indicating the 10-day transition). The grey crosses and lines indicate the observed Argo float deep initial locations and displacements in the region, respectively. (b, d, and f) Time evolution of the spread of the 100 trajectories measured by plus/minus the standard deviation of the zonal distances, by plus/minus the standard deviation of the meridional distances, and by the square of the zonal-meridional cross-distance, respectively. Distance of the trajectories are measured from the point of origin every ten days (cross, connected by dashed lines), following (9). (c and e) as (b and d) but for the variance and (f) is equivalent to (g). The dashed red lines is the best linear fit, which coefficient measured the diffusivities for the respective direction and is indicated in the title, following (10). . . . .</p>	47
6	<p><b>Diffusivity estimation from Argo floats.</b> (a-c) Zonal, meridional, and cross diffusivity coefficients (<math>\times 10^3 \text{ m}^2 \text{ s}^{-1}</math>). Note the non-linearity of the color scale reflecting low (below <math>2 \times 10^3 \text{ m}^2 \text{ s}^{-1}</math>) and high (above <math>2 \times 10^3 \text{ m}^2 \text{ s}^{-1}</math>) absolute values of diffusivities (i.e., linear from 0 to <math>2 \times 10^3 \text{ m}^2 \text{ s}^{-1}</math> and from 2 to <math>20 \times 10^3 \text{ m}^2 \text{ s}^{-1}</math> absolute values). The global mean values are indicated in the title. . . . .</p>	48
7	<p><b>Error in the diffusivity estimation from the linear fit.</b> (a-c) Error for the zonal, meridional, and cross diffusivity coefficients (% or <math>\times 10\%</math>). Except in a few specific locations the zonal and meridional errors remain below a few percents. The error for cross diffusivity coefficient is more important. . . . .</p>	49
8	<p><b>Area distributions of diffusivity coefficients.</b> (a-c) Zonal, meridional, and cross diffusivity values (<math>\times 10^3 \text{ m}^2 \text{ s}^{-1}</math>). Red and black histograms reflect distributions using <math>3^\circ \times 3^\circ</math> grid and <math>5^\circ \times 5^\circ</math> grid, respectively; solid black and dashed dark red lines reflect the expected values (means) using <math>3^\circ \times 3^\circ</math> grid and <math>5^\circ \times 5^\circ</math> grid, respectively; solid grey and dashed light red lines reflect the most typical values (medians) using <math>3^\circ \times 3^\circ</math> grid and <math>5^\circ \times 5^\circ</math> grid, respectively . . . . .</p>	50
9	<p><b>Rotated diffusivity estimation from Argo floats.</b> (a and b) Primary and secondary diffusivity coefficients (<math>\times 10^3 \text{ m}^2 \text{ s}^{-1}</math>) with their respective direction (lines, spaced by <math>3^\circ</math> for legibility). Note the non-linearity of the color scale reflecting low (below <math>2 \times 10^3 \text{ m}^2 \text{ s}^{-1}</math>) and high (above <math>2 \times 10^3 \text{ m}^2 \text{ s}^{-1}</math>) diffusivities (i.e., linear from 0 to <math>2 \times 10^3 \text{ m}^2 \text{ s}^{-1}</math> and from 2 to <math>20 \times 10^3 \text{ m}^2 \text{ s}^{-1}</math>). The global mean values are indicated in the title. . . . .</p>	51

10	<b>Diffusivity anisotropy measured by the ratio of primary to secondary diffusivity.</b> Values close to 1 show local isotropy of the diffusivity; values significantly higher than 1 show the significant dominance of the primary direction over the secondary one for diffusivity, and the local anisotropy of the diffusivity. (b and c) Scatter plots (dot) and density (contours), in term of the angle in radians from the north, of the primary diffusivity direction with the primary turbulent flow direction and with the mean flow direction, respectively. Density is computed as a normalized density on grid of $0.1\pi \times 0.1\pi$ radian angle. Contour interval are 0.1, thick purple lines are 0.5, and thin cyan and magenta lines are higher and lower values. . . . .	52
11	<b>Turbulent length scales.</b> Colors show (a-b) zonal and meridional turbulent length scales (km), following (12). . . . .	53
12	<b>Turbulent time scales.</b> Colors show (a-c) zonal, meridional, and cross turbulent time scales (day or $\times 4$ days), following (13). . . . .	54
13	<b>Fit of turbulent closures.</b> (a-b) Scatter plots (dots) of zonal and meridional diffusivities ( $\kappa_{xx}$ and $\kappa_{yy}$ , respectively) as a function of zonal and meridional turbulent velocity ( $\tilde{u}$ and $\tilde{v}$ , respectively). (c-e) Scatter plots (dots) of zonal, meridional, and cross diffusivity ( $\kappa_{xx}$ , $\kappa_{yy}$ , and $\kappa_{xy}$ , respectively) as a function of zonal, meridional, and co- turbulent velocity variance ( $\tilde{u}^2$ , $\tilde{v}^2$ , and $\tilde{c}^2$ , respectively). Red lines are the best linear fits (crossing zero), which coefficient (indicated in the title) estimates the best (a) zonal and (b) meridional turbulent length scale, following (12), or the best (c) zonal, (d) meridional, and (e) cross turbulent time scale, following (13). In each panel, the coefficient of determination of the linear fit ( $R^2$ – the proportion of variance explained by the fit) is indicated in the title. . . . .	55
14	<b>Area distributions of turbulent length and time scales.</b> (a) Area distribution of the (black) zonal and (red) meridional turbulent length scales as defined by (12) and shown in Fig. 11. (b) Area distribution of the (black) zonal and (red) meridional turbulent time scales as defined by (13) and shown in Fig. 12. (c) as in (b) but for the (grey) cross turbulent time scale. . . . .	56

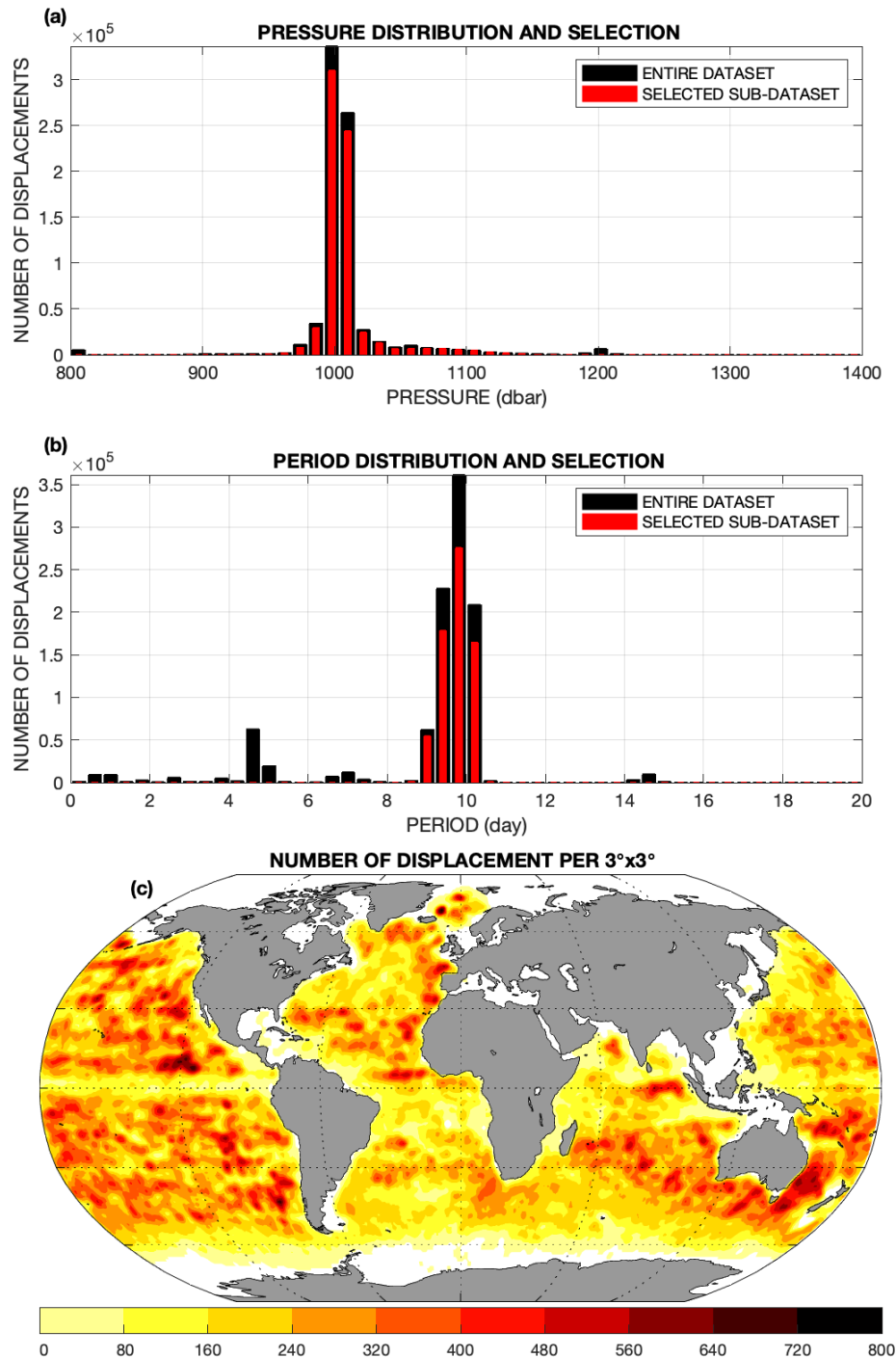


FIGURE 1: **Argo float deep displacement selection.** Distributions of (a) pressure and (b) period of Argo float deep displacements. Distributions are estimated from the entire ANDRO dataset (black) and after selecting displacements at a pressure between 950 and 1,150 dbar and with a period from 8.5 to 10.5 days (red). There are 1,041,054 displacements in the dataset and 675,575 displacements after selection. (c) Number of displacements from ANDRO dataset per  $3^\circ \times 3^\circ$  grid boxes for the selected 675,575 displacements (i.e., between 950 and 1,150 dbar and between 8.5 and 10.5 days).

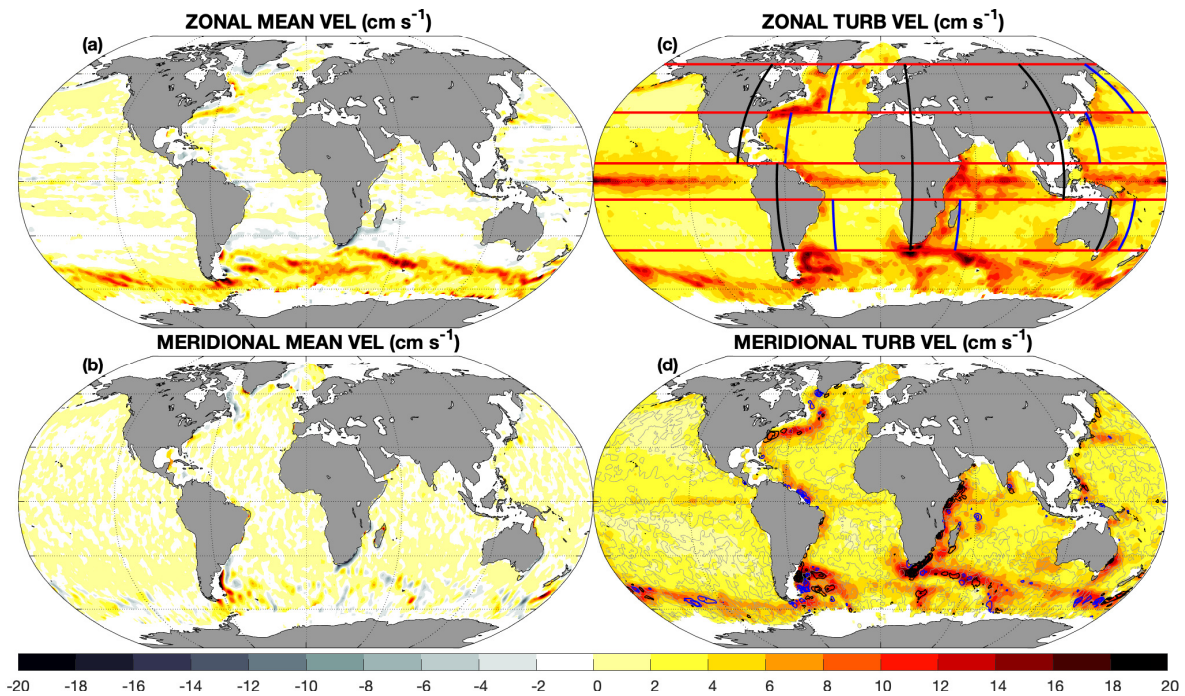


FIGURE 2: **Mean and turbulent zonal and meridional velocities.** Colors show (a and b) zonal and meridional mean and (c and d) turbulent velocities ( $\text{cm s}^{-1}$ ), following (1) and (2), respectively. (d) Contours show covariance of zonal and meridional velocities ( $\text{cm}^2 \text{s}^{-2}$ ), following (2). Velocities are computed each  $1^\circ \times 1^\circ$  as the velocity mean, standard deviation, and covariance within  $3^\circ \times 3^\circ$  grid boxes. Black, grey, and blue contours correspond to positive, zero, and negative values, with contour interval of  $20 \text{ cm}^2 \text{s}^{-2}$ . (c) The red and black lines show the latitudes and longitudes separating the regions used in Tab. 1. The blue lines show the limits between western boundaries and interiors.

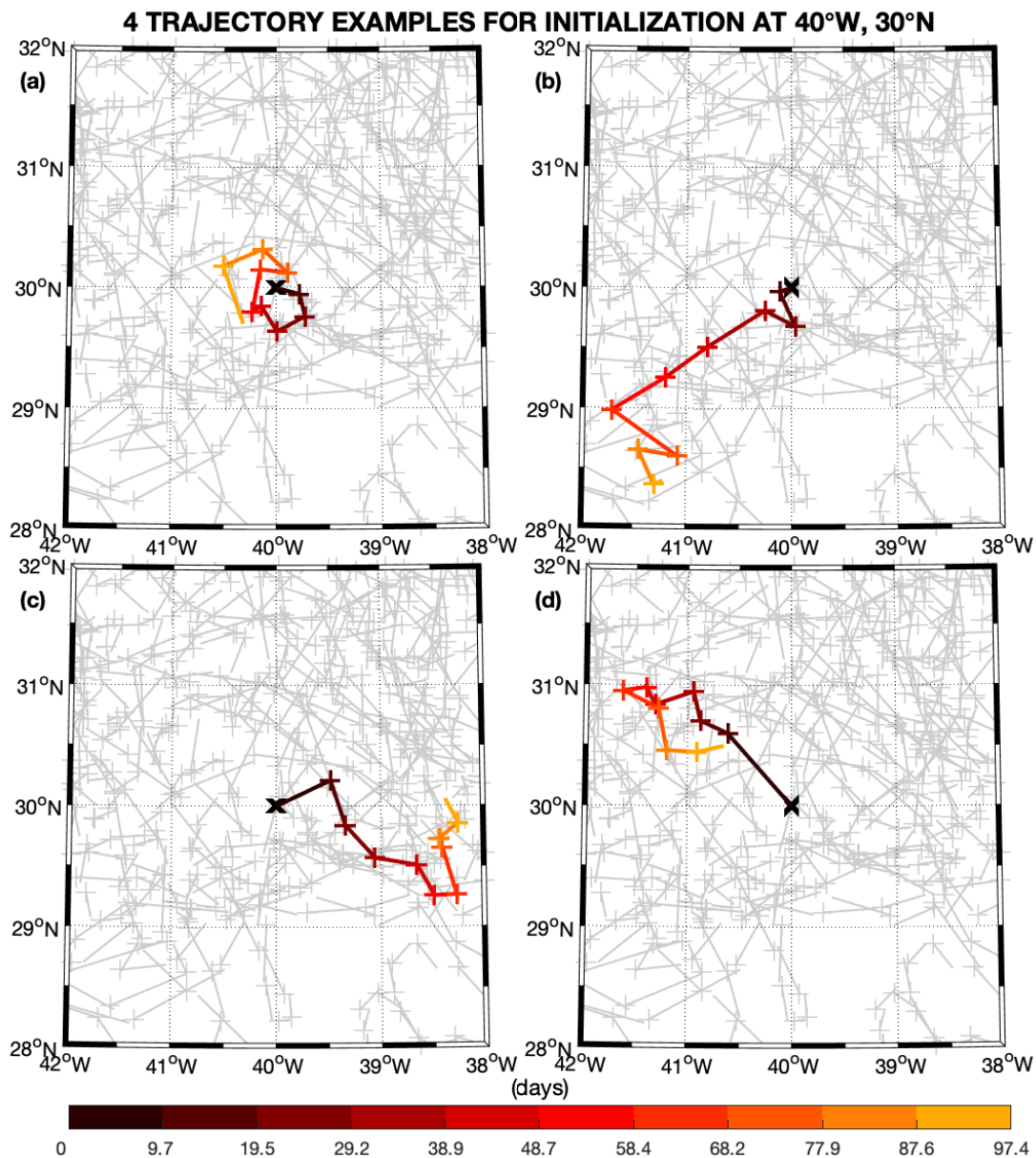
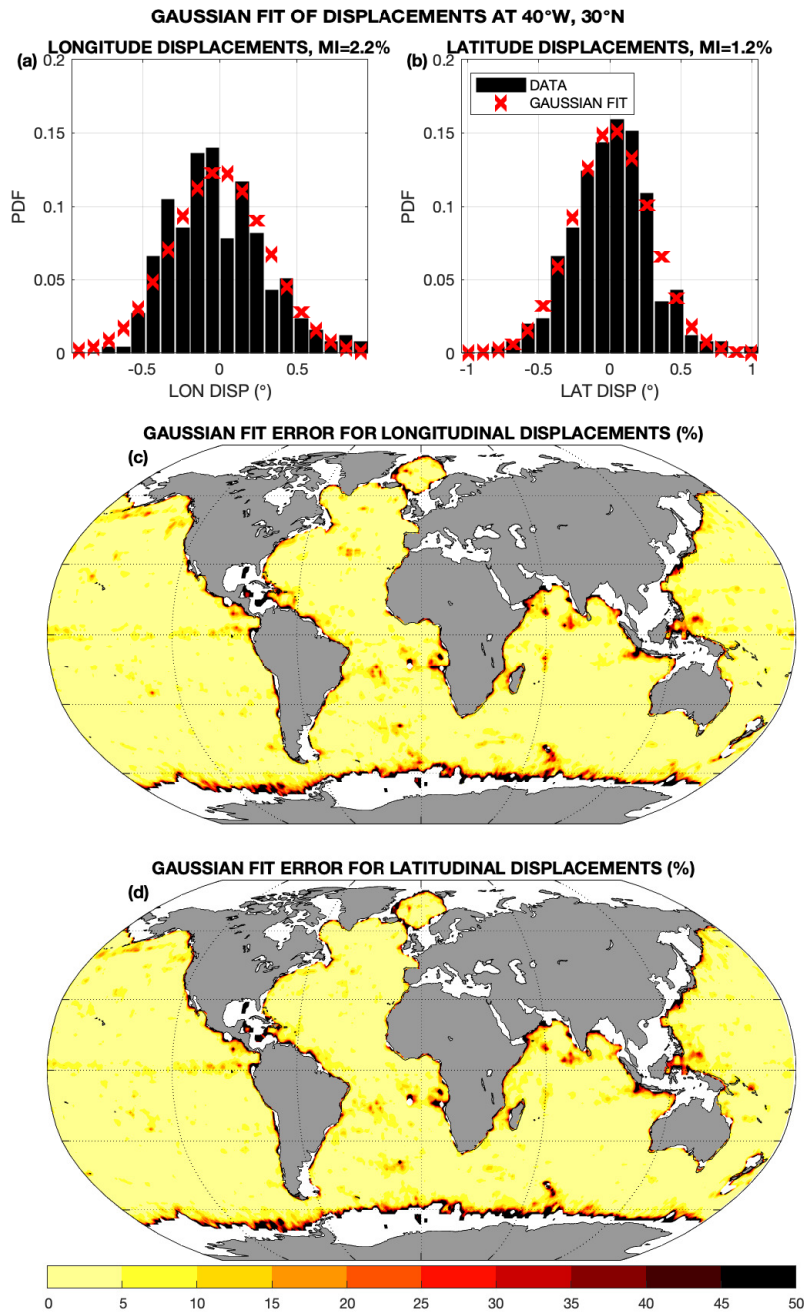


FIGURE 3: **Examples of 4 reconstructed pseudo-trajectories.** (a-d) The four continuous, likely trajectories are obtained using the analog method base on the ANDRO dataset (providing disconnected displacements from Argo floats during their journey at depth). They are initialized at 30°N, 40°W and used a 3°×3° grid to define the range of analogs. Crosses denote initial positions and lines denote displacements of both reconstructed continuous, likely trajectories (color) and observed disconnected Argo float displacements (grey). The color scale reflects the time evolution of the trajectories from 9.7 days to 97.4 days.



**FIGURE 4: Error estimation of the Gaussian fit approximation for the displacement probability density functions.** (a and b) Probability density function of longitudinal and latitudinal deep displacements (black bar), respectively, located at 30°N, 40°W. (red crosses) The Gaussian fits are computed using the mean and the variance of the distribution displacement. To compute the error of the Gaussian fits, we compute the Missing Information (MI). The Missing Information measures the error of the fit by computing the ratio of the Kullback-Leibler divergence to the Shannon Entropy. (c and d) Maps of the error of the Gaussian fits for longitudinal and latitudinal displacements, respectively.

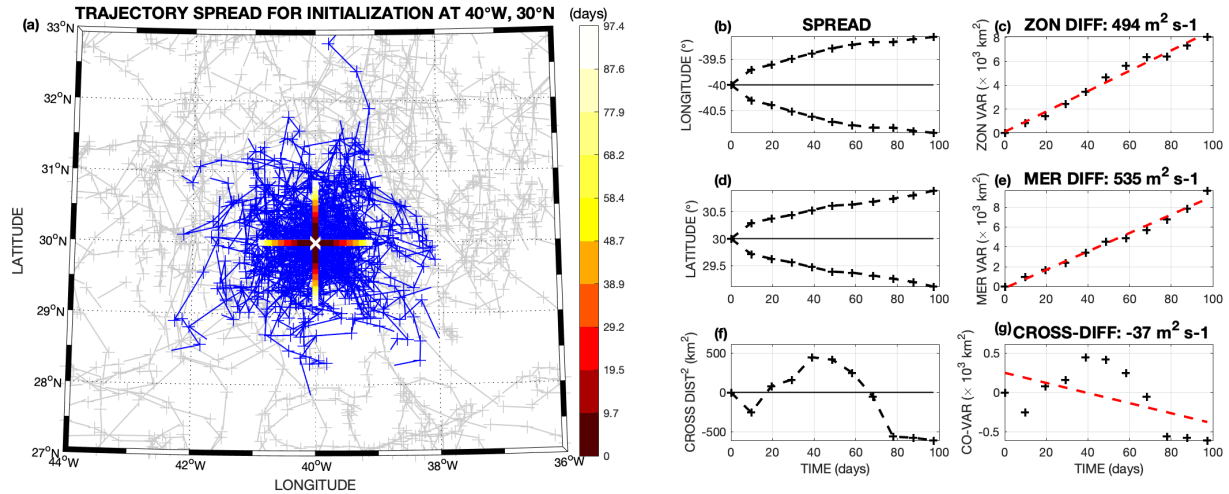


FIGURE 5: **Trajectory spread for initialization at  $30^{\circ}\text{N}$ ,  $40^{\circ}\text{W}$  and computation of the diffusivity coefficients.** (a) 100 individual pseudo-trajectories (blue crosses – separating 10-day transition – linked by lines), their mean position (white cross) and their plus/minus zonal and meridional standard deviation (horizontal and vertical thick lines, respectively, with colorscale – indicating the 10-day transition). The grey crosses and lines indicate the observed Argo float deep initial locations and displacements in the region, respectively. (b, d, and f) Time evolution of the spread of the 100 trajectories measured by plus/minus the standard deviation of the zonal distances, by plus/minus the standard deviation of the meridional distances, and by the square of the zonal-meridional cross-distance, respectively. Distance of the trajectories are measured from the point of origin every ten days (cross, connected by dashed lines), following (9). (c and e) as (b and d) but for the variance and (f) is equivalent to (g). The dashed red lines is the best linear fit, which coefficient measured the diffusivities for the respective direction and is indicated in the title, following (10).

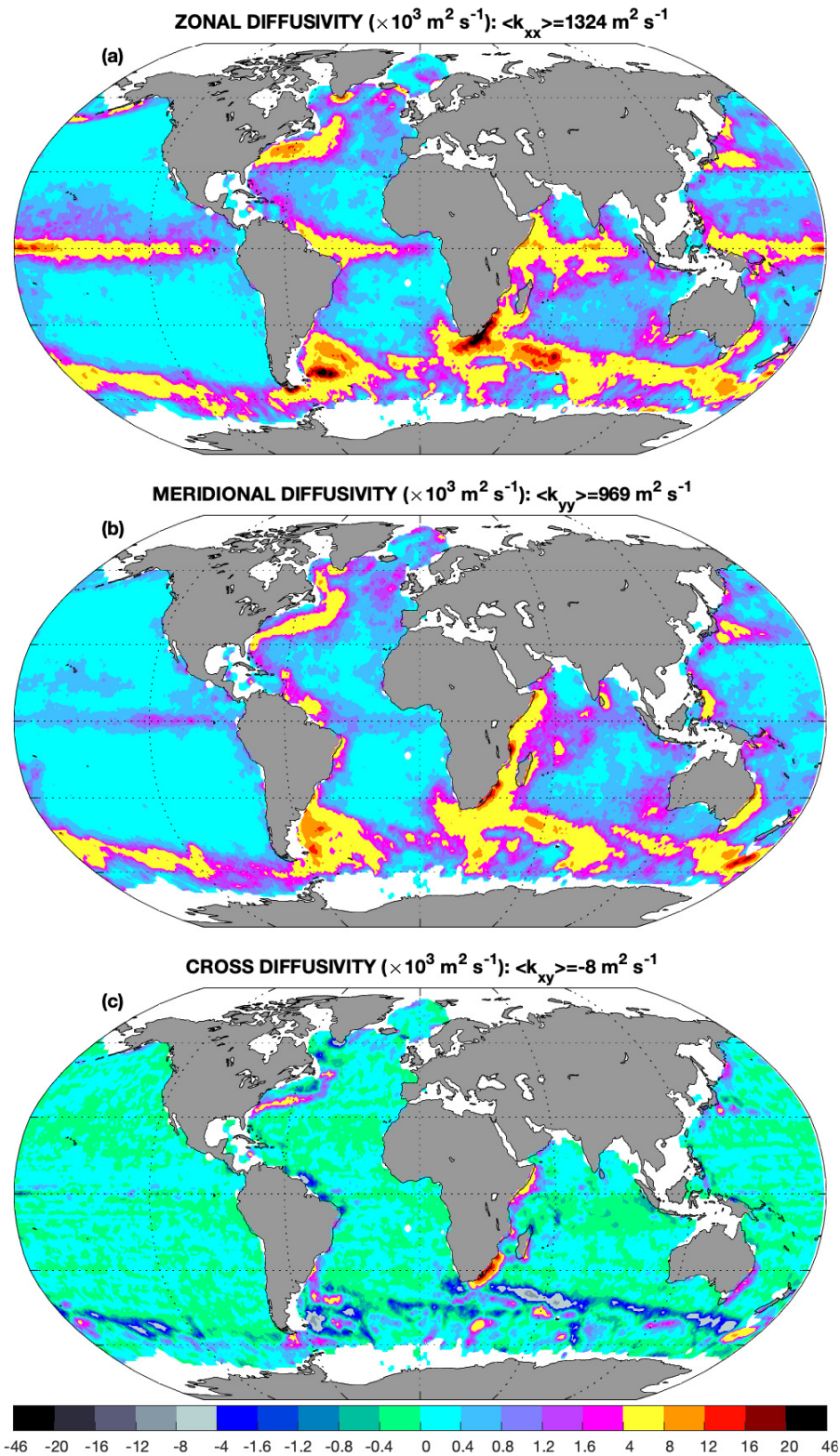


FIGURE 6: **Diffusivity estimation from Argo floats.** (a-c) Zonal, meridional, and cross diffusivity coefficients ( $\times 10^3 \text{ m}^2 \text{ s}^{-1}$ ). Note the non-linearity of the color scale reflecting low (below  $2 \times 10^3 \text{ m}^2 \text{ s}^{-1}$ ) and high (above  $2 \times 10^3 \text{ m}^2 \text{ s}^{-1}$ ) absolute values of diffusivities (i.e., linear from 0 to  $2 \times 10^3 \text{ m}^2 \text{ s}^{-1}$  and from 2 to  $20 \times 10^3 \text{ m}^2 \text{ s}^{-1}$  absolute values). The global mean values are indicated in the title.

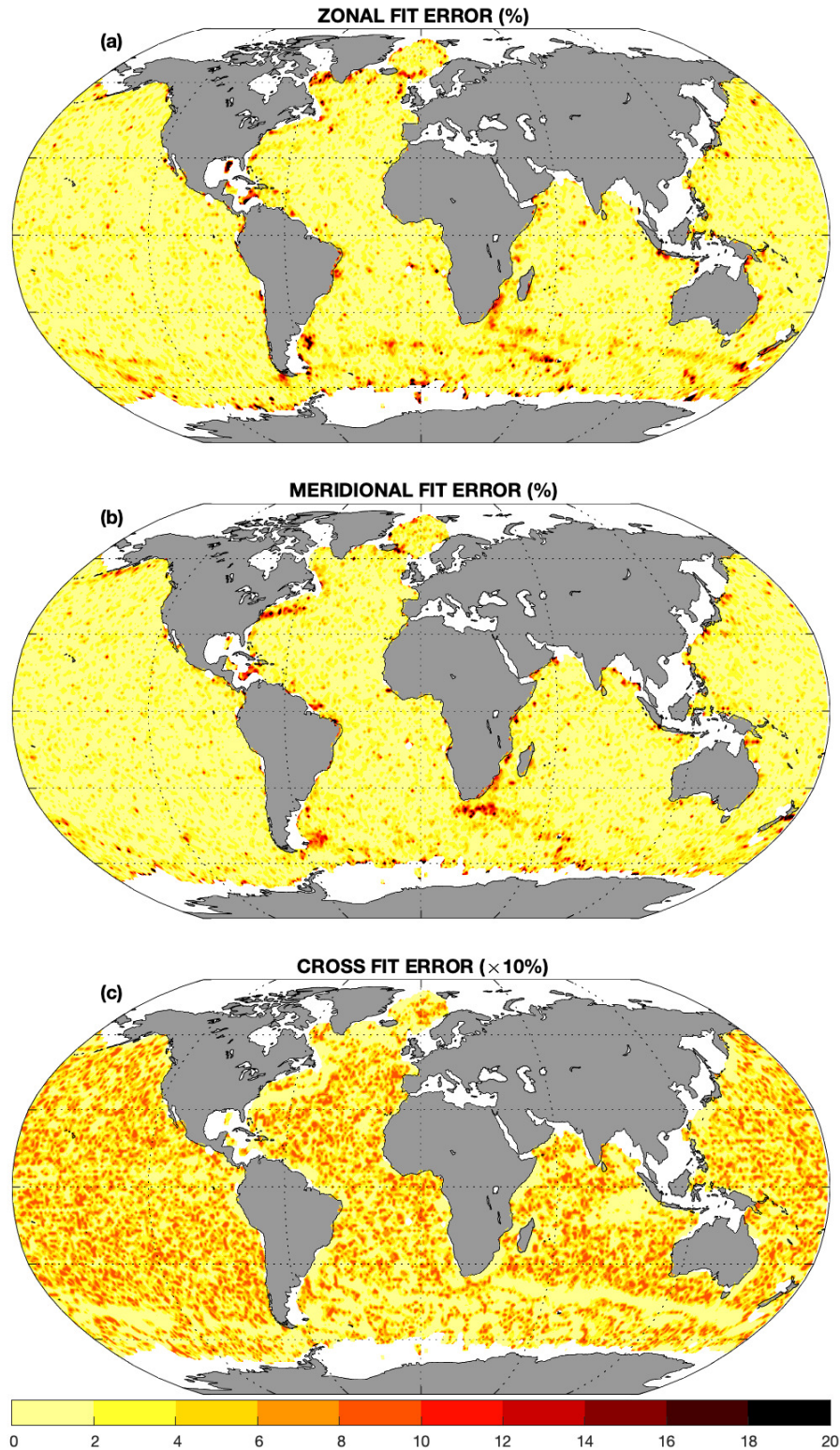


FIGURE 7: **Error in the diffusivity estimation from the linear fit.** (a-c) Error for the zonal, meridional, and cross diffusivity coefficients (% or  $\times 10\%$ ). Except in a few specific locations the zonal and meridional errors remain below a few percents. The error for cross diffusivity coefficient is more important.

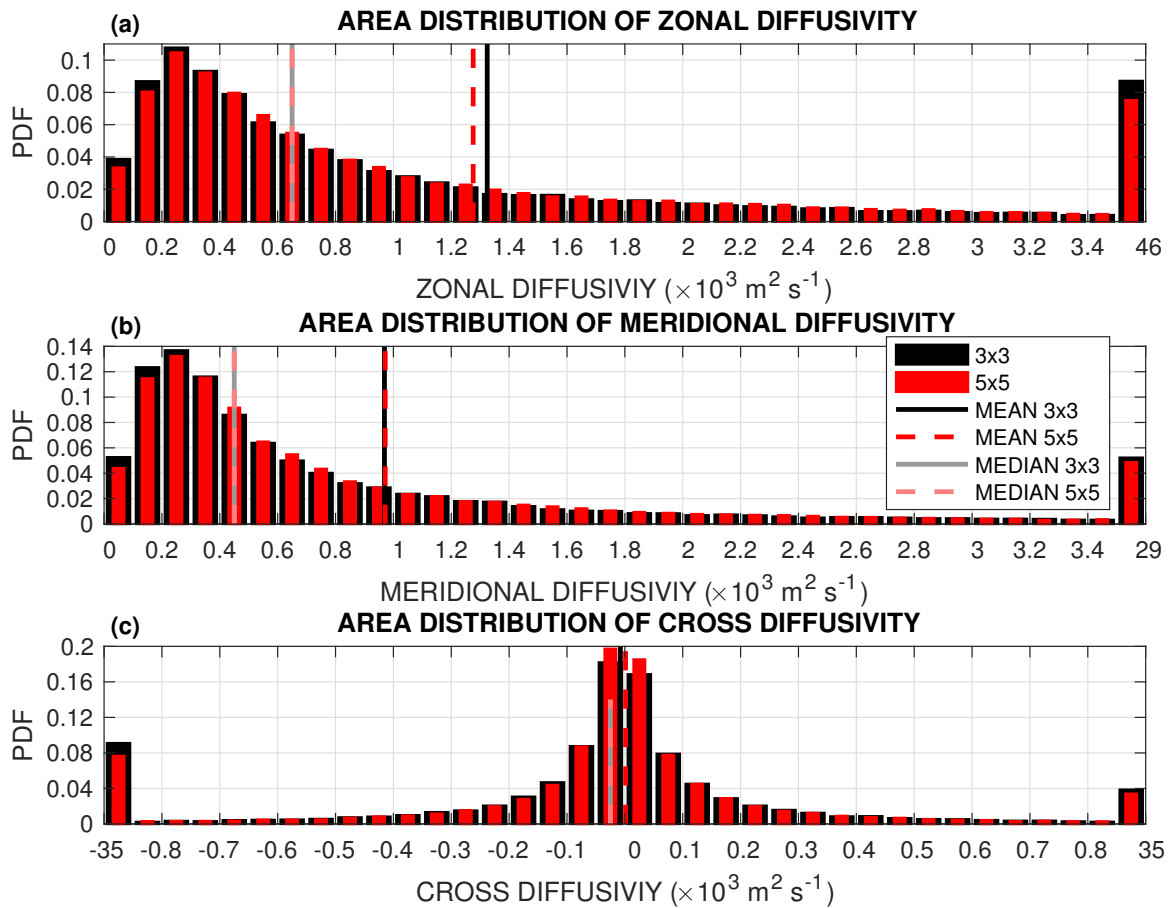


FIGURE 8: **Area distributions of diffusivity coefficients.** (a-c) Zonal, meridional, and cross diffusivity values ( $\times 10^3 \text{ m}^2 \text{ s}^{-1}$ ). Red and black histograms reflect distributions using  $3^\circ \times 3^\circ$  grid and  $5^\circ \times 5^\circ$  grid, respectively; solid black and dashed dark red lines reflect the expected values (means) using  $3^\circ \times 3^\circ$  grid and  $5^\circ \times 5^\circ$  grid, respectively; solid grey and dashed light red lines reflect the most typical values (medians) using  $3^\circ \times 3^\circ$  grid and  $5^\circ \times 5^\circ$  grid, respectively

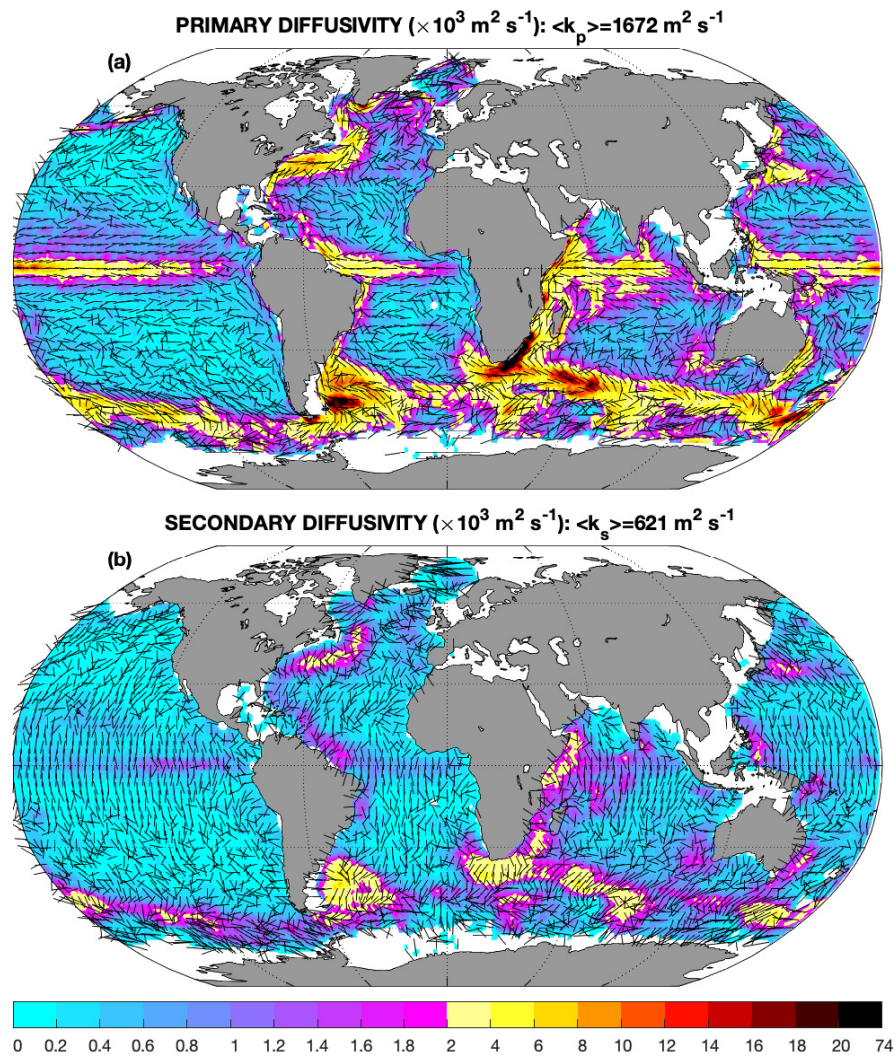


FIGURE 9: **Rotated diffusivity estimation from Argo floats.** (a and b) Primary and secondary diffusivity coefficients ( $\times 10^3 \text{ m}^2 \text{ s}^{-1}$ ) with their respective direction (lines, spaced by  $3^\circ$  for legibility). Note the non-linearity of the color scale reflecting low (below  $2 \times 10^3 \text{ m}^2 \text{ s}^{-1}$ ) and high (above  $2 \times 10^3 \text{ m}^2 \text{ s}^{-1}$ ) diffusivities (i.e., linear from 0 to  $2 \times 10^3 \text{ m}^2 \text{ s}^{-1}$  and from 2 to  $20 \times 10^3 \text{ m}^2 \text{ s}^{-1}$ ). The global mean values are indicated in the title.

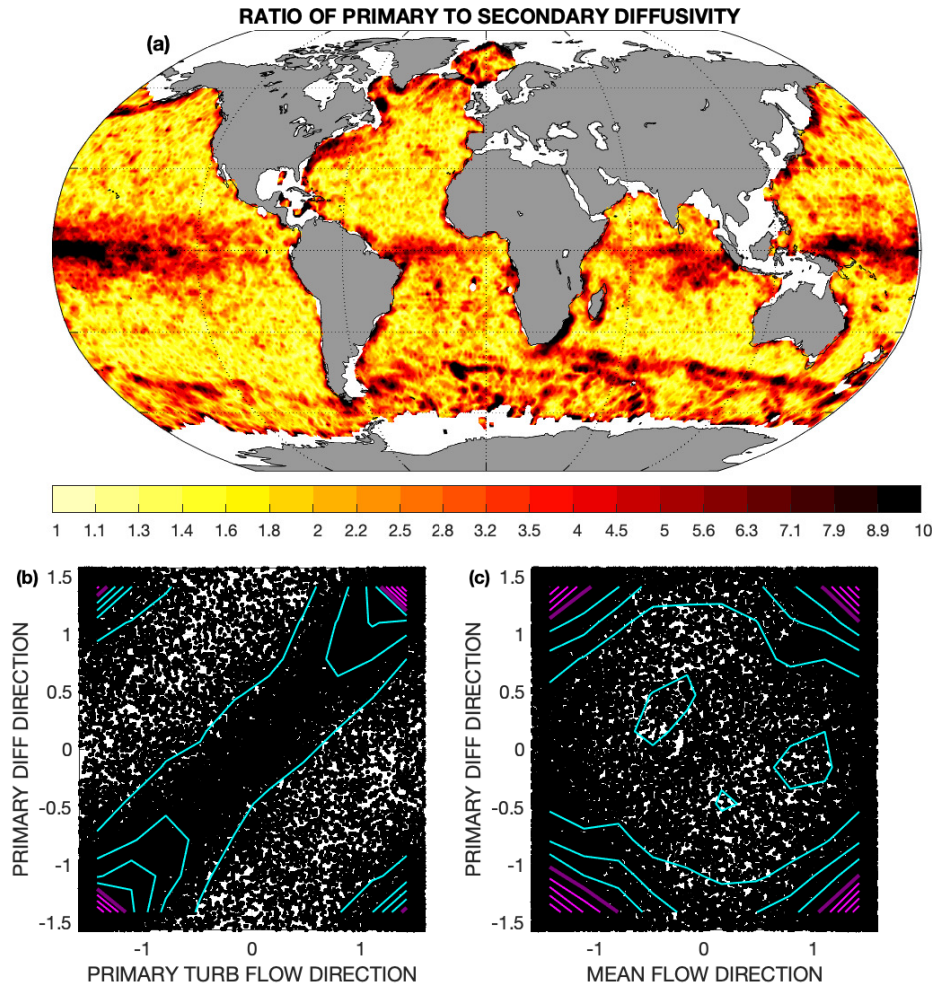


FIGURE 10: **Diffusivity anisotropy measured by the ratio of primary to secondary diffusivity.** Values close to 1 show local isotropy of the diffusivity; values significantly higher than 1 show the significant dominance of the primary direction over the secondary one for diffusivity, and the local anisotropy of the diffusivity. (b and c) Scatter plots (dot) and density (contours), in term of the angle in radians from the north, of the primary diffusivity direction with the primary turbulent flow direction and with the mean flow direction, respectively. Density is computed as a normalized density on grid of  $0.1\pi \times 0.1\pi$  radian angle. Contour interval are 0.1, thick purple lines are 0.5, and thin cyan and magenta lines are higher and lower values.

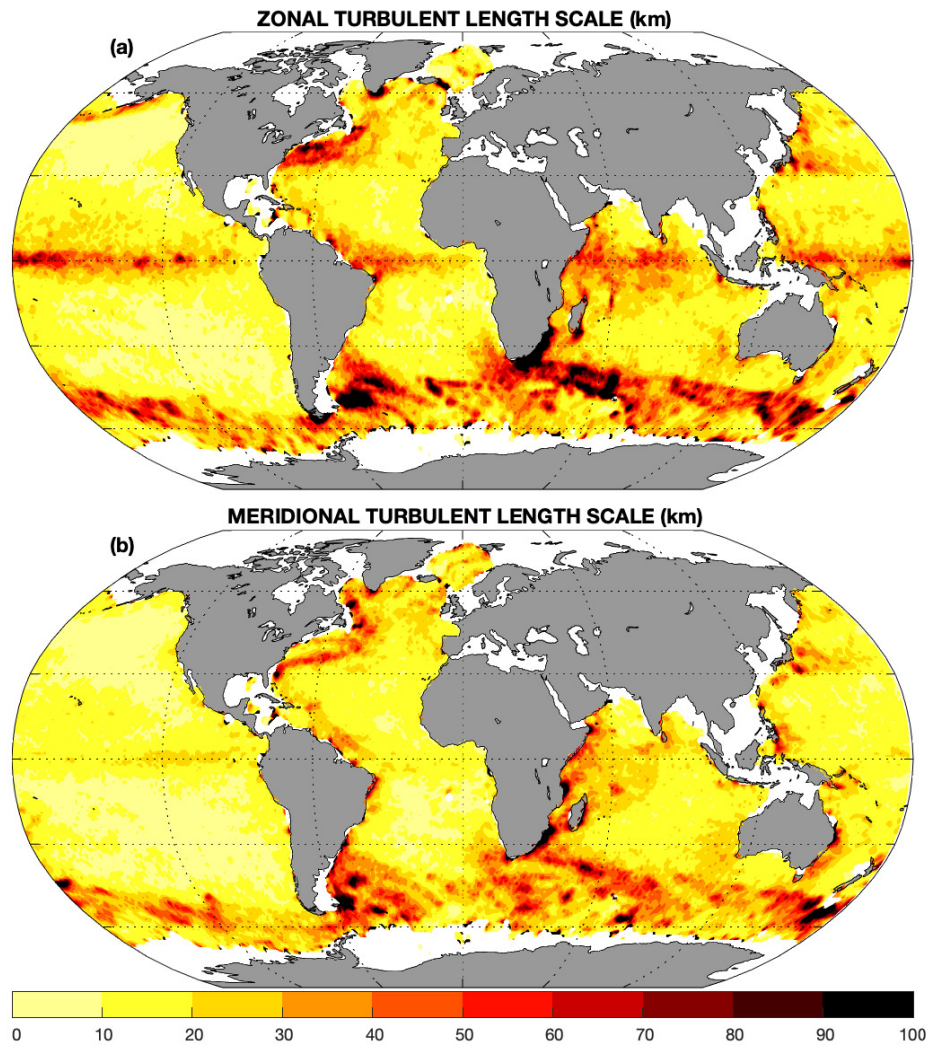


FIGURE 11: **Turbulent length scales.** Colors show (a-b) zonal and meridional turbulent length scales (km), following (12).

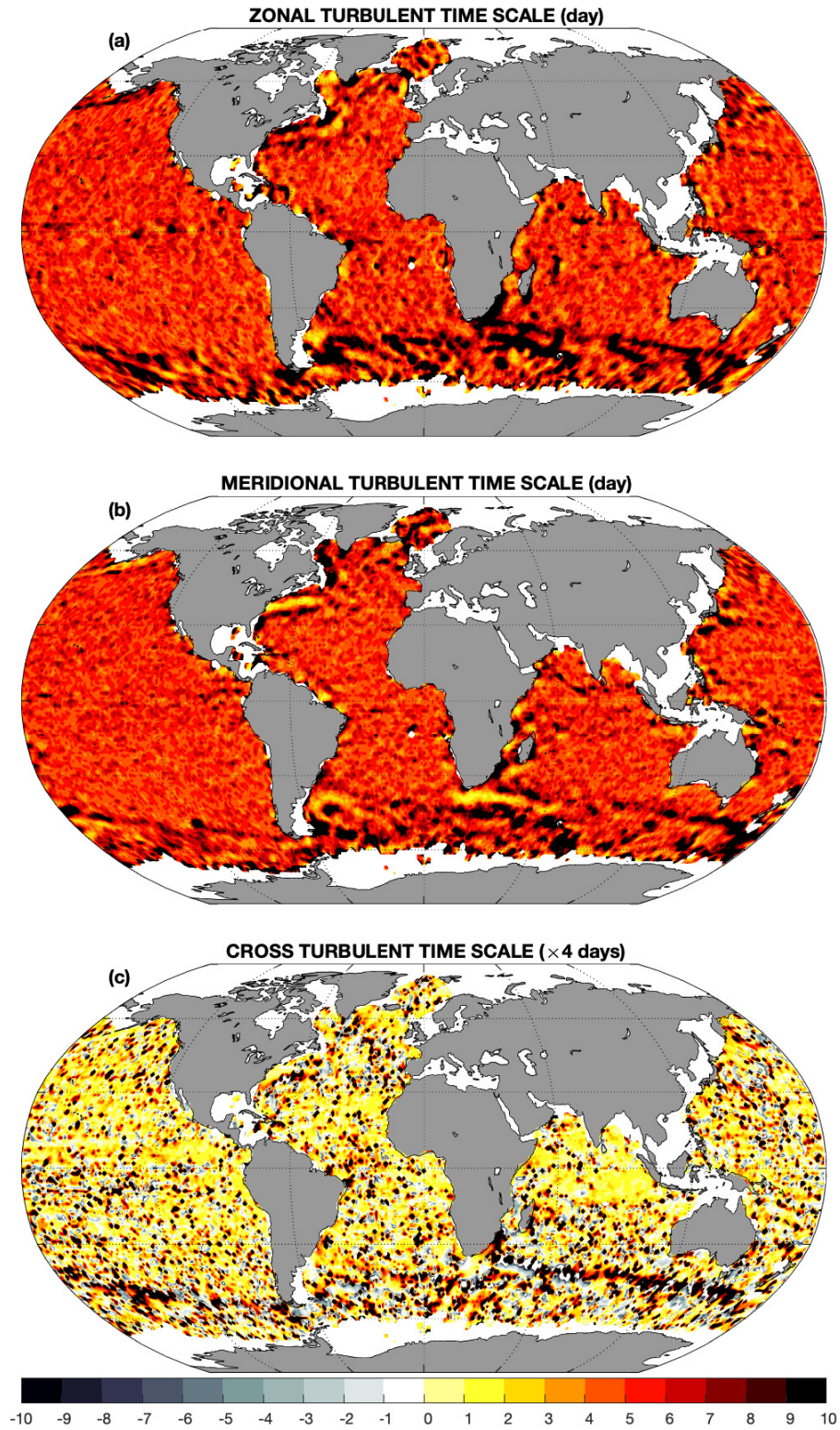


FIGURE 12: **Turbulent time scales.** Colors show (a-c) zonal, meridional, and cross turbulent time scales (day or  $\times 4$  days), following (13).

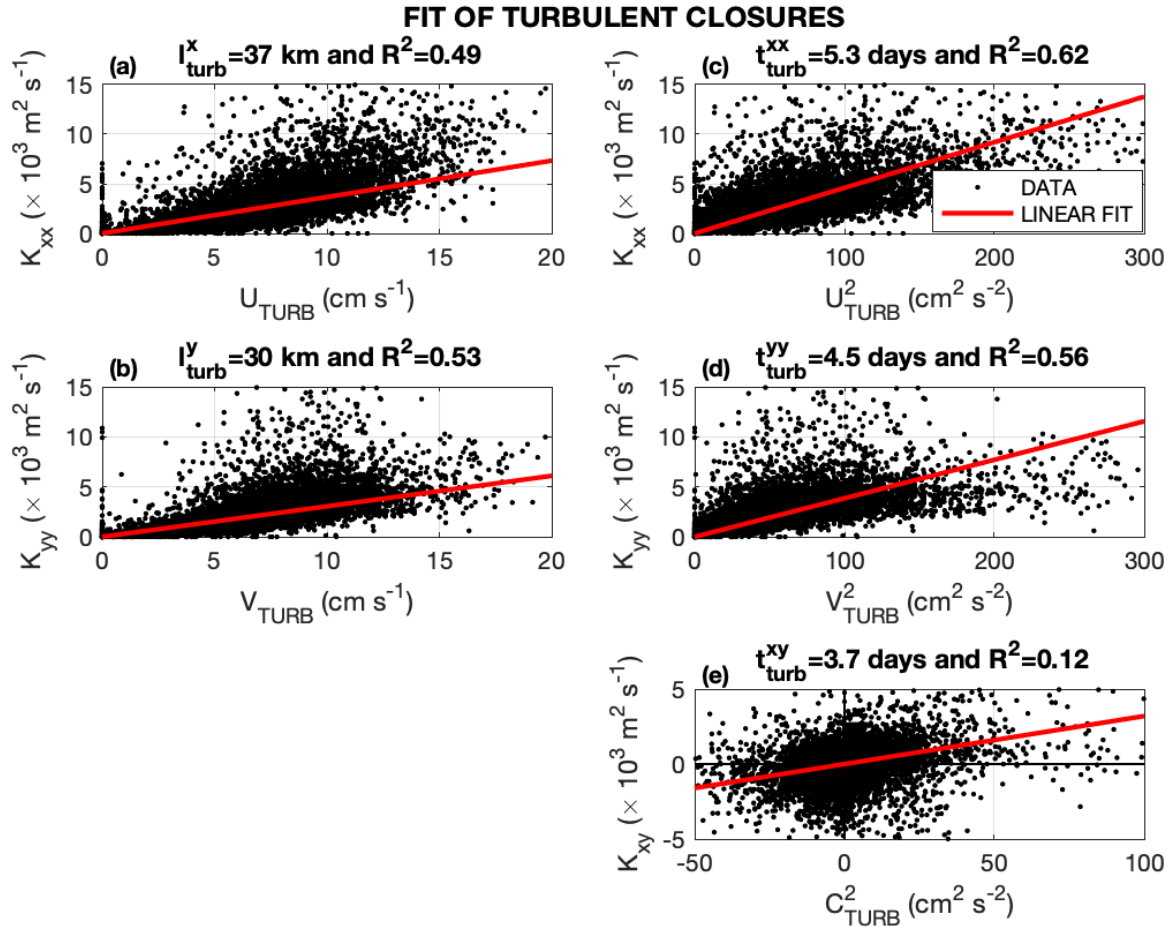


FIGURE 13: **Fit of turbulent closures.** (a-b) Scatter plots (dots) of zonal and meridional diffusivities ( $\kappa_{xx}$  and  $\kappa_{yy}$ , respectively) as a function of zonal and meridional turbulent velocity ( $\tilde{u}$  and  $\tilde{v}$ , respectively). (c-e) Scatter plots (dots) of zonal, meridional, and cross diffusivity ( $\kappa_{xx}$ ,  $\kappa_{yy}$ , and  $\kappa_{xy}$ , respectively) as a function of zonal, meridional, and co-turbulent velocity variance ( $\tilde{u}^2$ ,  $\tilde{v}^2$ , and  $\tilde{c}^2$ , respectively). Red lines are the best linear fits (crossing zero), which coefficient (indicated in the title) estimates the best (a) zonal and (b) meridional turbulent length scale, following (12), or the best (c) zonal, (d) meridional, and (e) cross turbulent time scale, following (13). In each panel, the coefficient of determination of the linear fit ( $R^2$  – the proportion of variance explained by the fit) is indicated in the title.

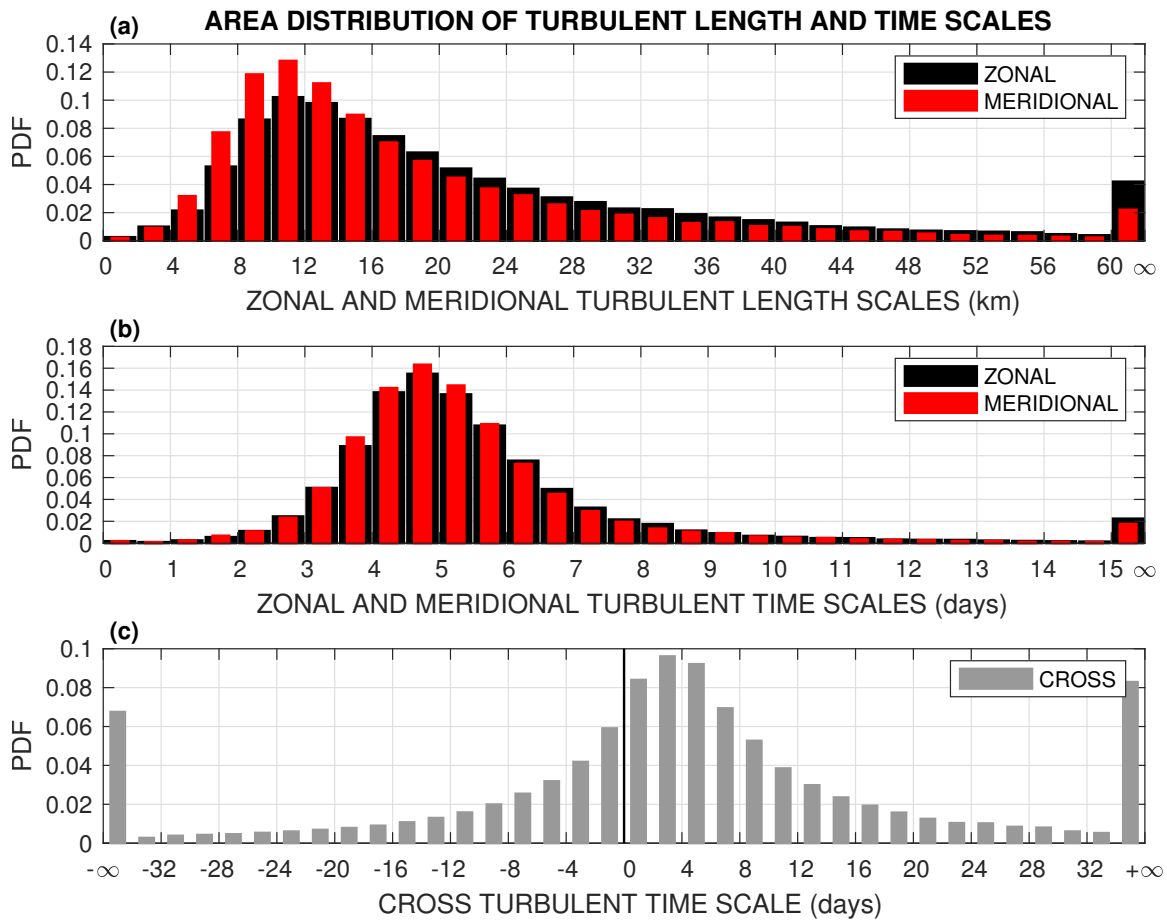


FIGURE 14: **Area distributions of turbulent length and time scales.** (a) Area distribution of the (black) zonal and (red) meridional turbulent length scales as defined by (12) and shown in Fig. 11. (b) Area distribution of the (black) zonal and (red) meridional turbulent time scales as defined by (13) and shown in Fig. 12. (c) as in (b) but for the (grey) cross turbulent time scale.

## List of Tables

- 1 **Regional values of diffusivities and closure.** Values are averaged over the globe (global) and 18 regions : SubPolar North Atlantic Western Boundary and Interior (SP-NA-WB and SP-NA-I, respectively); SubTropical North Atlantic Western Boundary and Interior (SP-NA-WB and SP-NA-I, respectively); SubTropical South Atlantic Western Boundary and Interior (ST-SA-WB and ST-SA-I, respectively); Equatorial Atlantic, Indian Ocean and Pacific (EQ-A, EQ-IO, and EQ-P, respectively); SubTropical Indian Ocean Western Boundary and Interior (ST-IO-WB and ST-IO-I, respectively); SubPolar North Pacific Western Boundary and Interior (SP-NP-WB and SP-NP-I, respectively); SubTropical North Pacific Western Boundary and Interior (ST-NP-WB and ST-NP-I, respectively); SubTropical South Pacific Western Boundary and Interior (ST-SP-WB and ST-SP-I, respectively); and the Southern Ocean (SO). The regions are split between the subpolar, subtropical, and equatorial regions (following 38°S, 10°S, 10°N, 38°N, and 66°N), between the Atlantic, Indian and Pacific region (following 90°W and 65°W for the North and South Atlantic, respectively, 20°E, and 115°E and 145°E for the North and South Pacific, respectively), and between the ocean western boundaries and interiors (35°W for the subpolar North Atlantic, 60°W and 30°W for subtropical North and South Atlantic, respectively, 50°E for the subtropical Indian Ocean, 170°W for the subpolar North Pacific, and 138°W and 160°W for subtropical North and South Pacific, respectively). The regions are shown in Fig. 2c. . . . .

58

TABLE 1: **Regional values of diffusivities and closure.** Values are averaged over the globe (global) and 18 regions : SubPolar North Atlantic Western Boundary and Interior (SP-NA-WB and SP-NA-I, respectively); SubTropical North Atlantic Western Boundary and Interior (SP-NA-WB and SP-NA-I, respectively); SubTropical South Atlantic Western Boundary and Interior (ST-SA-WB and ST-SA-I, respectively); Equatorial Atlantic, Indian Ocean and Pacific (EQ-A, EQ-IO, and EQ-P, respectively); SubTropical Indian Ocean Western Boundary and Interior (ST-IO-WB and ST-IO-I, respectively); SubPolar North Pacific Western Boundary and Interior (SP-NP-WB and SP-NP-I, respectively); SubTropical North Pacific Western Boundary and Interior (ST-NP-WB and ST-NP-I, respectively); SubTropical South Pacific Western Boundary and Interior (ST-SP-WB and ST-SP-I, respectively); and the Southern Ocean (SO). The regions are split between the subpolar, subtropical, and equatorial regions (following 38°S, 10°S, 10°N, 38°N, and 66°N), between the Atlantic, Indian and Pacific region (following 90°W and 65°W for the North and South Atlantic, respectively, 20°E, and 115°E and 145°E for the North and South Pacific, respectively), and between the ocean western boundaries and interiors (35°W for the subpolar North Atlantic, 60°W and 30°W for subtropical North and South Atlantic, respectively, 50°E for the subtropical Indian Ocean, 170°W for the subpolar North Pacific, and 138°W and 160°W for subtropical North and South Pacific, respectively). The regions are shown in Fig. 2c.

	$\kappa_{xx}$ (m <sup>2</sup> s <sup>-1</sup> )	$\kappa_{yy}$ (m <sup>2</sup> s <sup>-1</sup> )	$\kappa_p$ (m <sup>2</sup> s <sup>-1</sup> )	$\kappa_s$ (m <sup>2</sup> s <sup>-1</sup> )	$l_{\text{turb}}^x$ (km)	$l_{\text{turb}}^y$ (km)	$t_{\text{turb}}^{xx}$ (days)	$t_{\text{turb}}^{yy}$ (days)
Global	1324	969	1672	621	24	19	113.5	8.4
SP-NA-WB	2444	1906	3217	1134	35	31	8.5	6.8
SP-NA-I	806	783	1096	493	20	20	25.0	8.8
ST-NA-WB	1227	1055	1703	579	24	22	6.6	6.9
ST-NA-I	614	585	765	435	16	15	5.1	5.0
EQ-A	1322	718	1520	520	23	17	7.1	5.2
ST-SA-WB	1309	1704	2126	887	23	28	5.6	8.2
ST-SA-I	633	557	778	413	15	13	5.2	5.7
EQ-IO	1833	1166	2183	816	27	21	6.2	5.3
ST-IO-WB	5443	4015	7750	1708	64	49	10.4	7.4
ST-IO-I	890	824	1108	607	19	18	5.4	5.1
SP-NP-WB	960	839	1296	503	23	20	10.7	6.4
SP-NP-I	352	233	421	164	11	9	7.3	6.3
ST-NP-WB	925	812	1224	514	22	20	7.5	7.4
ST-NP-I	564	399	636	326	17	13	297.3	6.4
EQ-P	1707	544	1800	450	26	15	5.4	5.3
ST-SP-WB	1195	1860	2228	828	24	28	13.0	6.0
ST-SP-I	313	282	380	215	11	10	5.1	5.0
SO	2234	1784	2936	1082	35	28	333.6	17.8